ERA report series

16 ERA-20CM: a twentieth century atmospheric model ensemble

Hans Hersbach, Carole Peubey, Adrian Simmons, Paul Poli,
Dick Dee and Paul Berrisford

Series: ERA report series

A full list of ECMWF Publications can be found on our web site under:
http://www.ecmwf.int/publications/

Contact: library@ecmwf.int

European Centre for Medium Range Weather Forecasts
Shinfield Park, Reading, RG2 9AX, England

Abstract

This paper describes an ensemble of ten atmospheric model integrations for the years 1899 to 2009, performed at the European Centre for Medium-Range Weather Forecasts. Horizontal spectral resolution is T159 (about 125 km in grid-point space), using 91 levels in the vertical from the surface up to 1 Pa, and a time step of one hour. This ensemble, denoted by ERA-20CM, forms the first step toward a 20th century reanalysis within ERA-CLIM, a three-year European funded project involving nine partners.

Sea-surface temperature and sea-ice cover are prescribed by an ensemble of realizations (HadISST2), as recently produced by the Met Office Hadley Centre within ERA-CLIM. Variation in these realizations reflect uncertainties in the available observational sources on which this product is based. Forcing terms in the model radiation scheme follow CMIP5 recommendations. Any effect of their uncertainty is neglected. These terms include solar forcing, greenhouse gases, ozone and aerosols. Both the ocean-surface and radiative forcing incorporate a proper long-term evolution of climate trends in the 20th century, and the occurrence of major events, such as the El Niño-Southern Oscillations and volcanic eruptions.

No atmospheric observations were assimilated. For this reason ERA-20CM is not able to reproduce actual synoptic situations. The ensemble is, however, able to provide a statistical estimate of the climate. Overall, the temperature rise over land is in fair agreement with the CRUTEM4 observational product. Over the last two decades the warming over land exceeds the warming over sea, which is consistent with models participating in the CMIP5 project, as well with the ECMWF ERA-Interim reanalysis. Some aspects of warming and of the hydrological cycle are discerned, and the model response to volcanic eruptions is qualitatively correct.

The results of ERA-20CM are freely available, embracing monthly-mean fields for many geophysical parameters, and synoptic fields for a small, essential subset.

1 Introduction

Warming of the climate system over the course of the past century or more is unequivocal, and is projected to continue, bringing with it substantial socio-economic impacts (Pachauri and Reisinger, 2007). Our current understanding on the detailed feedbacks in our climate system is still far from complete. Models and data records are improving and the climate-change signal is clear when considered over a long period of time. However, climate trends are the residue of individually large components of the physical equations that govern the Earth system. On the seasonal and synoptic time scale these trends are small compared to the annual cycle and the variability of the weather, in particular. This puts a very high demand on the quality of our models and the observing network.

To make projections of our future climate based on anticipated changes in e.g., greenhouse-gas concentrations, it is necessary to look at the past climate, and how well we are able to represent it in a model context.

The reconstruction of the past climate requires an adequate network of historical observations. During the 20th century the observing system has evolved dramatically. Although synoptic observations of surface wind and pressure and sea-surface temperature have been available for more than one 150 years (see e.g., Woodruff *et al.* (2011)), their distribution has been sparse during most of this period. Upper-air data have a shorter history. Sporadic kite observations in the early 1900s, later followed by pilot balloons and aircraft observations and the introduction of the radiosonde in the 1930s allowed for a progressively more complete sensing of the atmosphere (see e.g. Stickler *et al.* (2010)). The conventional observing system

had a boost in the International Geographical Year (1957), when the observing system for the Southern Hemisphere was improved significantly. Substantial amounts of satellite data has been available since the 1980s.

Besides an incomplete and geographically highly uneven distribution, a large amount of early data has never been digitized, and as a result never been re-used. Worldwide, several data recovery initiatives have emerged to improve on this situation, often in coordination with the Atmospheric Circulation Reconstructions over the Earth (ACRE) project (http://www.met-acre.org). However, the current difficult economic situation has put a strain on the continuation of some of these activities.

One project that is involved in the recovery, digitization and usage of observational datasets suitable for global climate studies, with focus on the past 100 years is ERA-CLIM. This three-year initiative (2011-2013) is funded under the Seventh Framework Programme of the European Union, and undertaken by a consortium of eight partners from Europe and one from Chile. It is coordinated by ECMWF. A concise overview of the project is presented in Dee *et al.* (2012).

A specific goal of ERA-CLIM is to improve the quality and consistency of climate observations through global reanalyses. For this a few sets of pilot reanalyses are being produced at ECMWF. Such reanalyses provide a powerful tool to dynamically inter-validate observations, by using the laws of physics that relate them. Reanalysis is a well established method to reconcile historical data sets. The same model context is used throughout, which filters out discontinuities due to model improvements that are present in the operational products of numerical weather production centres (NWP) such as ECMWF. Major global reanalysis programmes take place at the NOAA National Centers for Environmental Prediction (NCEP), the Japan Meteorological Agency (JMA), the NASA Global Modeling and Assimilation Office (GMAO) and ECMWF. A general overview and description of current developments at ECMWF are described in Dee *et al.* (2012).

Despite the consistency in time of the model that glues together observations into global analysis fields, the explosive expansion of the observing system itself can have a significant effect on the average representation of low-frequency variability of such fields, This, when interpreted without care can lead to incorrect climate signals (see e.g., Bengtsson *et al.* (2004)).

Careful inter-calibration, and or a robust bias correction scheme between various data sets is crucial. However, the reduction or knowledge of systematic model errors is equally important. In sparsely observed regions, such as the Southern Hemisphere in the early 1900s, reanalysis fields do not contain much information from actual observations, and mainly reflect the behaviour of the model climate. If the model climatology is biased, the introduction of a new observing source may result in an artificial shift in analysis fields. Besides the level of sophistication in model physics and advection schemes, systematic effects are also imposed by external forcing. For an atmospheric model these include a prescription of the ocean surface (sea-surface temperature and sea ice) and substances that affect radiation budgets (e.g., greenhouse gases and aerosols). These quantities have evolved significantly during the 20th century.

The first pilot study in ERA-CLIM embodies an ensemble of model-only integrations. It is denoted by ERA-20CM and its setup and results are the subject of this paper. In the literature such model ensembles are often denoted by AMIP (Atmospheric Model Intercomparison Project, Gates (1992)). The rationale behind ERA-20CM is to allow for a separation between the behaviour of the free model climate and the influence of the ingestion of an evolving set of observations, which latter is envisaged in subsequent ERA-CLIM pilot reanalyses (see e.g. Poli *et al.* (2013)). No synoptic meteorological data are assimilated, and all observational information is incorporated in its boundary conditions and forcing. An ensemble of ten realizations is integrated from January 1 1899 to December 31 2009, using a recent release of the ECMWF Integrated Forecasting System (IFS), but at a reduced resolution (T159)

compared to the operational configuration (T1279).

It is important that the forcing terms represent a proper evolution during the 20th century, since these have an influence on the evolution of the (model) climate. At the ocean surface, each ERA-20CM member is forced by one realization of sea-surface temperature (SST) and sea-ice cover (SIC) as recently provided by the Met Office Hadley Centre. This new ensemble of SST and SIC, called HadISST2 (Kennedy *et al.* (2013); Titchner and Rayner (2013); Rayner *et al.* (2013)), is one of the deliverables of ERA-CLIM. Variation among the HadISST2 realizations reflects uncertainties in observational sources.

The radiative forcing follows recommendations from the Coupled Model Intercomparison Project Phase 5 (CMIP5, Taylor *et al.* (2012)), carried out under the auspices of the World Climate Research Programme (WCRP). Research groups were invited to use these forcings in well-defined AMIP and CMIP simulations, with the aim to contribute towards the IPCC Fifth Assessment Report (AR5).

The ECMWF IFS system was adapted at various points to allow for the incorporation of these forcings. Some of these adaptations had recently been provided by the EC-Earth consortium (Hazeleger *et al.*, 2012). This group, which is formed by a number of ECMWF member states, focuses on long-range coupled atmosphere ocean sea-ice simulations (CMIP) based on the ECMWF atmospheric model and NEMO ocean model. The adaptations used in ERA-20CM involve variations in the solar forcing, the evolution of ozone, greenhouse gases, tropospheric aerosols, and volcanic (stratospheric) aerosols. Evolution in vegetation, urbanisation, leaf-area index and albedo have not been taken into account. The prescribed external radiative forcing is the same for all ten ERA-20CM members, i.e., its uncertainty is neglected. Any variation in radiation, such as from clouds, originates from differences between the atmospheric state in the ensemble.

The paper is organized as follows. Section 2 gives a concise overview of the ECMWF forecast model. Adaptations for the incorporation of CMIP5 radiative and HadISST2 ocean-surface forcing is described in Section 3. Some sensitivity studies regarding these forcings are presented here as well. Details on the production and archiving are presented in Section 4. Sections 5-8 describe various aspects of the long-term evolution of the ERA-20CM ensemble. Conclusions and an outlook are formulated in Section 9.

2 Concise description of the ECMWF forecast model

At ECMWF all data assimilation and forecasting activities share the same model environment, called the Integrated Forecasting System (IFS). Adaptations and improvements are incorporated about twice a year. ERA-20CM is a variation of the atmosphere and ocean-wave forecast model components of Cy37r3, an IFS release that was used in the operational ECMWF stream between 15 November 2011 and 19 June 2012. The only difference with Cy37r3 comes from the adaptations that were required to allow for the ingestion of HadISST and CMIP5 forcing. Documentation and a historical overview of IFS may be found at http://www.ecmwf.int/research/ifsdocs.

The dynamical core of the atmospheric model is based on a spectral representation of the basic dynamical variables, a hybrid sigma-pressure vertical coordinate, and a semi-Lagrangean semi-implicit time stepping scheme. IFS supports a range of (horizontal and vertical) resolutions and integration time steps. The ERA-20CM model integrations are based on a 1-hour time step and a spectral T159 horizontal resolution, which corresponds to approximately 125 km spacing on a reduced Gaussian grid. There are 91 levels in the vertical, ranging from a height of 10 m above the surface to 1 Pa (about 80 km). This embraces roughly 51 levels in the troposphere, 31 in the stratosphere and 9 in the mesosphere.

The physical core provides a parametrization for radiative transfer, turbulent diffusion and interaction

with the surface, subgrid-scale orographic drag, non-orographic gravity wave drag, moist convection, clouds, and surface/soil processes. Some relevant details on the IFS radiation scheme are provided in Section 3.2. Due to a high computational expense, the radiation scheme is usually run at a lower horizontal and temporal resolution. For ERA-20CM it was based on a spectral T63 resolution and called once every three hours, which is the default for a T159 configuration.

The ocean-wave model is a derivative from WAM (Komen *et al.*, 1994), which provides an evolution of the 2-dimensional energy density of ocean waves, called wave spectrum. It is two-way coupled with the atmosphere. Physical parametrization involves wave growth due to surface stress (wind) and some other atmospheric quantities, non-linear interaction between waves, and dissipation due to white-capping and bottom friction. The dependence of the surface roughness on the wave state (Janssen, 1991) influences the evolution of the atmosphere. ERA-20CM uses a wave spectrum with 25 frequencies and 12 directions on a $1.5^o \times 1.5^o$ grid, and an advection and interaction time step of 15 minutes.

Although the seasonal component of IFS allows for a two-way coupling between ocean and atmosphere, in an atmosphere only configuration, such as ERA-20CM and the ECMWF operational 10-day forecast system, sea surface temperature and sea-ice cover are prescribed. For dates from October 2008 such fields are obtained from the Met Office OSTIA product, while for earlier dates an NCEP SST and SIC analysis product is used. For ERA-20CM these are replaced by the HadISST2 product (see Section 3.1). The ocean acts as an infinite source of energy regarding the latent and sensible heat flux and long-wave radiation at its surface. Any net downward surface flux will not affect the ocean state. As a result the long-term evolution of the atmospheric energy content is steered by the prescribed SST. Although systematic errors in the model energy budget may affect temperature profiles, the net effect on climate trends will be drained into the ocean.

Atmospheric mass is not exactly conserved in the IFS model. The effect is small, and is estimated to increase mass by a few tenths of a percent per year (Berrisford *et al.*, 2011b). This will add up to unacceptable levels in a 100-year model integration that does not use external information on mass (such as surface pressure observations). IFS provides an option to correct for this, which was used in the ERA-20CM configuration, where the dry mass was corrected on a three-hourly basis.

3 ERA-20CM external forcing

3.1 HadISST2

As part of the ERA-CLIM project, the Met Office Hadley Centre has delivered an improved sea-surface temperature and sea-ice concentration product, called HadISST2 (Kennedy *et al.* (2013); Titchner and Rayner (2013); Rayner *et al.* (2013)). It is a thoroughly revised version of the widely used HadISST1 product (Rayner *et al.*, 2003), as e.g. adopted by ERA-40 (Uppala *et al.*, 2005) . HadISST2 comprises of an ensemble of 10 realizations of daily SST and SIC on a $0.25^o \times 0.25^o$ regular lat-lon grid.

The SST fields are based on in situ SST observations from version 2.5 of the International Comprehensive Ocean-Atmosphere Data Set (ICOADS, Woodruff *et al.* (2011)), improved AVHRR data from the Pathfinder and retrievals from ATSR reprocessing. Variation in the HadISST2 realizations reflect uncertainties in the observational sources and bias adjustments. Two different analysis windows were supplied to ERA-CLIM; a monthly window ('monthly' set) supplied from 1 January 1899 to 15 December 2010, and a five-day window ('pentad' set) supplied from 1 January 1961 to 15 December 2010. Daily fields were obtained by temporal interpolation of analysis fields from adjacent months with weights such that

the average of all daily fields in one analysis window equals the monthly analysis again. First a high-resolution climatology was created from all available data, from which monthly and pentad anomalies were calculated. Near-globally complete fields were estimated using a multistep process. First, an iterative, Empirical Orthogonal Function (EOF) based reconstruction technique was applied to estimate the large scale variability. Even for the early 20th century this first step allowed, e.g. for the reconstruction of an El-Niño condition based on a limited number of ship tracks in the Southern Hemisphere and Tropical Pacific, only. Second, residuals from the large scale reconstruction were analysed using a local optimal interpolation scheme. The 10 realizations were drawn from the posterior probability distributions of the analysed fields. Details may be found in Kennedy *et al.* (2013).

Details on the construction of the SIC analyses may be found at Titchner and Rayner (2013). There is no variation between the members, i.e., no uncertainty estimate is provided for this quantity.

During the ERA-CLIM project, two versions have been delivered; HadISST.2.0.0.0 (December 2011) and later HadISST.2.1.0.0 (October 2012), each embracing a monthly and a pentad set, i.e., four products in total. The SST component of HadISST.2.1.0.0 has benefited from a newer version of the ATSR data, and SIC is based on a new sea ice concentration data set. In addition, cubic interpolation was used to create the daily fields from the monthly fields, rather than linear as used for HadISST.2.0.0.0. ERA-20CM is based on the monthly set of version HadISST.2.0.0.0, since that was the version that was available at the start of its production. The remainder of this paper mainly focuses on this product.

The native format of HadISST2 is NetCDF. At ECMWF all fields were converted to GRIB format using cdo (https://code.zmaw.de/projects/cdo), and were archived in the ECMWF Meteorological Archival and Retrieval System (MARS). This was performed for all four flavours, i.e., the pentad and monthly sets for both versions.

3.1.1 Some characteristics

The SST and SIC GRIB fields were subject to some basic diagnostics. For each of the ten HadISST2 realizations, as well as for their ensemble mean and spread, daily averages were calculated for a number of areas and timeseries were produced. An example is provided in Figure 1, which displays the evolution of the ensemble mean SST for two regions and ensemble spread for one region. Panel (a) clearly shows an initial decrease in the global average SST during the first decade of the 20th century, followed by a steady increase up to the mid 40s, a flat plateau until the late 70s and an increase afterwards. A similar plot for the Eastern Tropical Pacific (ETP) resolves the 20th-century El Ninõ and La Niña events (panel (c)). The steady decrease in ensemble spread (panel (b) of Figure 1) reflects the improvement of the conventional observing system over time. Interesting are the temporary increases that coincide with the two world wars. The sudden drops in spread in 1985 and 2008 mark the introduction of AVHRR and reprocessed ATSR data, respectively. Peaks in the spread during this satellite era indicate the temporary unavailability of such data.

Global fields of the monthly mean ensemble spread in SST (colours) and the occurrence of any SIC (grey) are presented in Figure 2. The difference between panel (a) for September 1900 and (b) for September 2000 indicates the evolution over a period of 100 year. It clearly shows a general decrease in sea-ice extent. The increase in confidence levels on SST is obtained everywhere. Note that by far the largest uncertainties occur near dynamically active regions, such as the Gulf Stream, the Agulhas Current, the Kuroshio Extension and the ETP. Smaller, though much larger-scale uncertainties occur over the remaining areas. These large-scale perturbations are found to have a large temporal correlation and persist in individual realizations for decades. They originate from a consistent choice in bias-uncertainty

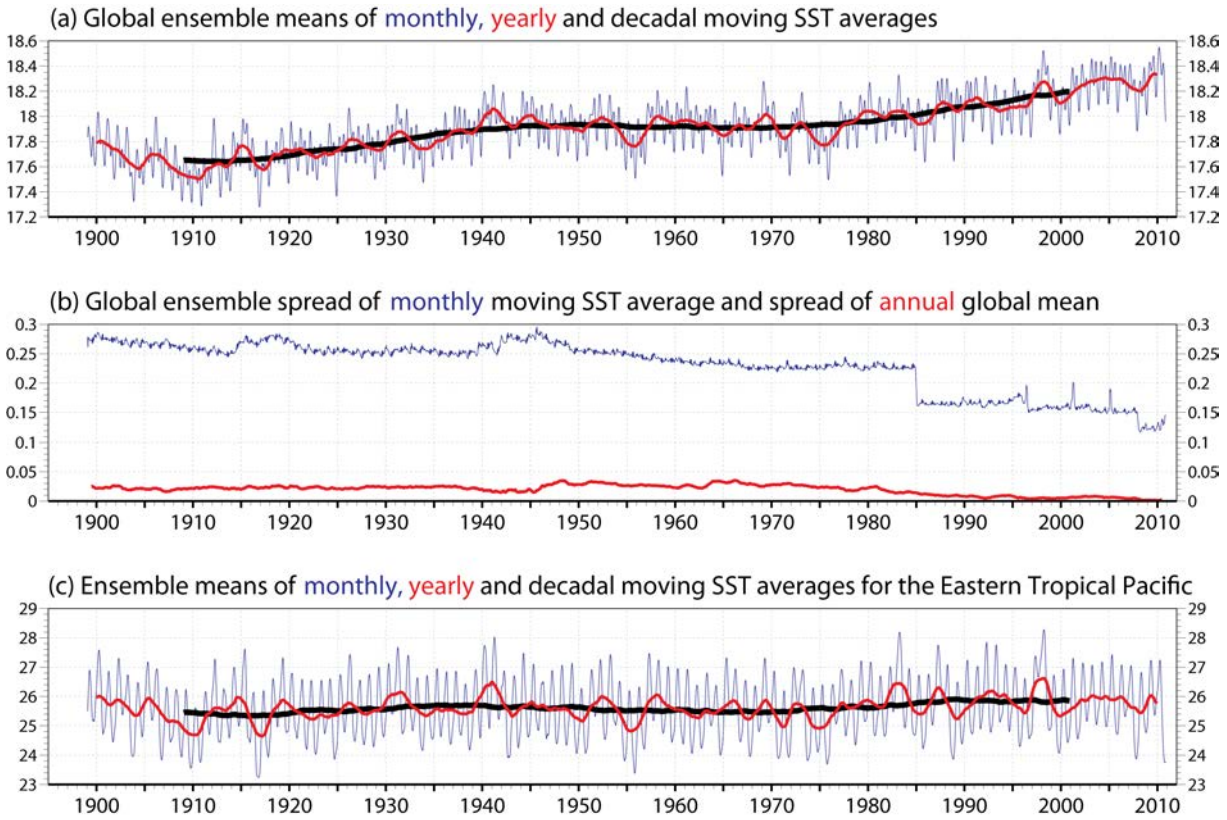

Figure 1: Time-series of HadISST.2.0.0.0 data for (a) global average of the SST ensemble mean (blue: monthly, red: yearly, black: decadal moving average) (b) Global average of the SST ensemble spread (blue: monthly moving average) and spread of the annual global mean SST (red) (c) as (a) but limited to the Eastern Tropical Pacific.

projected onto the EOF's. They dominate domain-averaged values. For this reason the difference in area-averaged SST between realizations is consistent over time (not shown).

The locally stronger small-scale perturbations, however, are much more random, and fluctuate between realizations within months. They tend to dominate area-averaged values of the ensemble spread. Analysis fields for dates at the start of the analysis window are an average of the analysis fields of adjacent analyses, which leads to interference between the small-scale perturbations. For this reason, the ensemble spread appears noticeably smaller at those dates (i.e., the first of each month for the monthly set) than for dates halfway through the analysis windows (the 15th of each month; not shown).

3.1.2 Ingestion in ERA-20CM

As mentioned in Section 2, the operational ECMWF model relies on an external SST and SIC product. These external fields are usually provided on a regular lat-lon grid, and have to be regridded to the ECMWF native reduced-Gaussian grid. This step is performed in a dedicated SST analysis by means of bi-linear interpolation. Local differences in the land-sea mask between the native and ECMWF grid are taken into account. For instance, the HadISST2 SIC product has missing values over the Ilchner-Ronne Ice Shelf and Amery Ice Shelf in the Antarctic, while SST has not. The ECMWF model treats these areas as land ice, so both SIC and SST are set to undefined here, i.e., the strip of SST south of SIC, as visible in Figure 2, is removed. Climatological values (based on one-month lagged ERA-40 2m-temperature) are

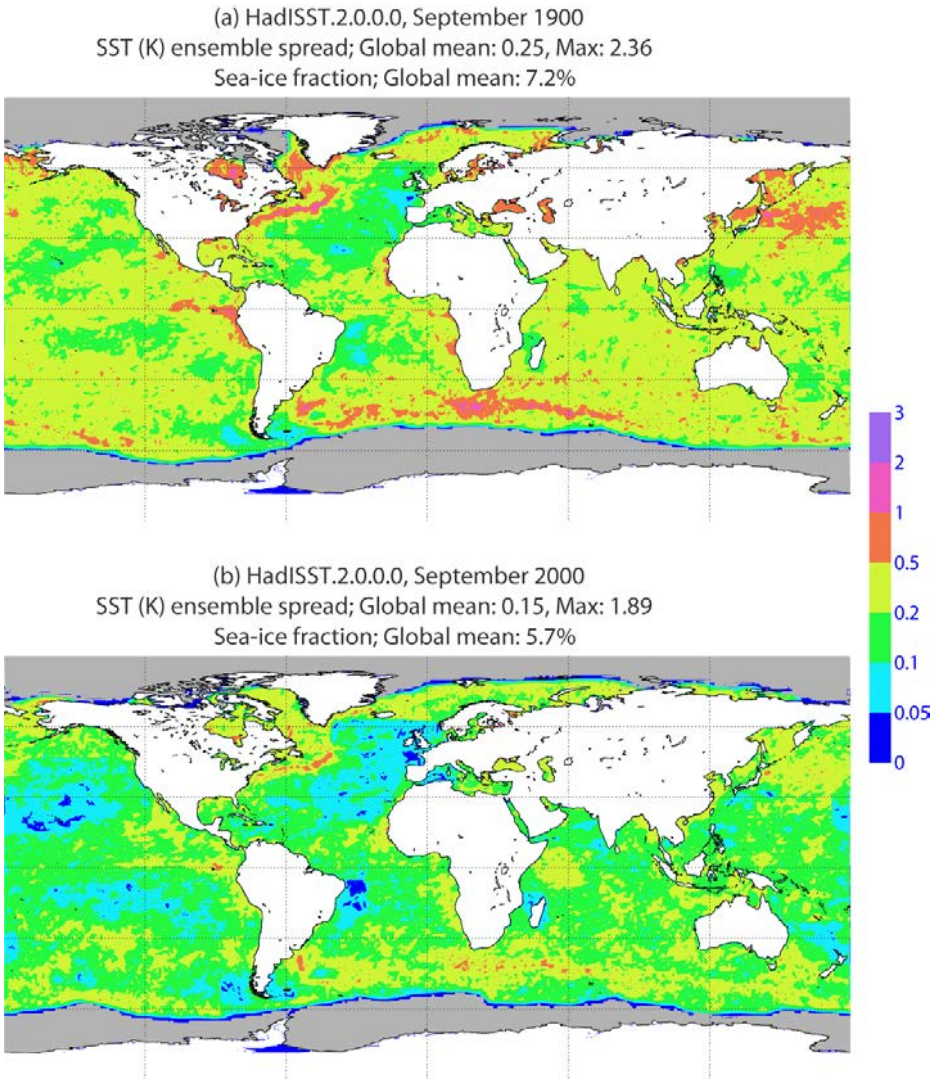

Figure 2: Monthly mean of HadISST.2.0.0.0 SST ensemble spread (colour scale, in K) and the extent of sea ice during the month (grey) for (a) September 1900 and (b) September 2000.

used for lakes that are resolved by the ECMWF model but unresolved by the external product. HadISST2 resolves the Great Lakes and the Caspian Sea.

In addition, the SST analysis step imposes some adjustments and consistency checks between SST and SIC. For HadISST2 such checks appear to remove sea ice from the Baltic Sea and The Great Lakes. Since the HadISST2 SST and SIC products were determined with great care, this adjustment is most probably incorrect. For this reason consistency checks and adjustments were disabled. Only a resetting to zero for SIC below 20% was retained, since this is desirable for the ECMWF surface parametrization.

IFS was adapted such that the HadISST2 product could be ingested. The choice of consistency checks is controlled with a new switch that is only activated for HadISST2. As explained in Kennedy *et al.* (2013) the ten provided HadISST2 realizations are the result of a random drawing from an, in principle large SST ensemble. They are all equally likely. The connection with ERA-20CM ensemble members is shown in Table 1. Since all 10 members are independent, and none of them is special, the choice of

ERA-20CM ensemble member	0	1	2	3	4	5	6	7	8	9
HadISST2.0.0.0 realization	103	1	119	120	129	135	19	28	34	6

Table 1: Relation between HadISST2.0.0.0 realization and ERA-20CM ensemble member

allocation has no effect on the statistical properties of ERA-20CM.

3.2 ECMWF radiation scheme and CMIP5 forcing

The IFS radiation is based on the McRad scheme (Morcrette *et al.*, 2008). It uses 14 spectral intervals in the short-wave (solar) and 16 in the long-wave (thermal) spectrum. It is based on the Rapid Radiation Transfer, which was originally developed at AER, Inc. Cloud effects are parametrized by the Monte-Carlo Independent Column Approximation (McICA). McRad has been part of IFS since Cy32r2, when it replaced the previous scheme by Morcrette (1991).

Incoming solar radiation is attenuated by absorbing gases, comprising water vapour, carbon dioxide (CO_2), a number of other greenhouse gases and ozone, and is scattered by molecules (Rayleigh scattering), aerosols and cloud particles. For water vapour, the radiation scheme uses prognostic information produced by the forecast model. For greenhouse gases, ozone and aerosols, prescribed climatological information is used instead. Prognostic ozone is available but has not been used in the radiation scheme so far, since coupling between ozone and radiation has been found to increase temperature errors in the stratosphere.

A century-long integration, such as ERA-20CM, requires that the climatological input fields follow the observed 20th century evolution. A state-of-the-art and standardized set of such long-term forcing fields is available from the World Climate Research Programme (WCRP) initiative CMIP5. For some quantities, such as the long-term evolution of CO_2 , IFS Cy37r3 provides already a long-term prescription. For some other quantities, like solar irradiance, CMIP5 recommendations are available from the ECMWF seasonal forecast system (System 4, Molteni *et al.* (2011)), which was introduced in IFS Cy36r4, and therefore available (via switches) in Cy37r3 as well. For ozone, synergy was kindly obtained from the EC-Earth consortium (Hazeleger *et al.*, 2012). This group of ECMWF member states had already addressed the CMIP5 adaptation of forcing fields in IFS before the start of ERA-CLIM. The at that time available EC-EARTH v2.2 is a branched version of IFS Cy31r1. This is before the introduction of McRad, however, and for this reason only part of EC-EARTH adaptations could be merged into the ERA-20CM branch. For remaining quantities IFS was adapted.

Adaptations for ERA-20CM allow for the ingestion of CMIP5 data from 1850 onwards, and include future projections up to the year 2100 via provided Representative Concentration Pathways (RCP). For recent dates ERA-20CM follows RCP2.6. These options were originally provided as a branched version of Cy36r4, but became part of standard IFS from Cy37r2 onwards, where they can be activated at will. It does not affect the operational setting of IFS.

3.2.1 Incoming solar forcing (total irradiance)

In IFS, solar forcing is incorporated via the Total Solar Irradiance (TSI): the amount of solar radiation integrated over all wavelengths at a distance of one astronomical unit (AU). It is rescaled to the actual solar distance and redistributed over the 14 short-wave frequency bands taking into account the local solar elevation. The operational configuration uses a fixed TSI of 1366 Wm^{-2}, and ERA-Interim and

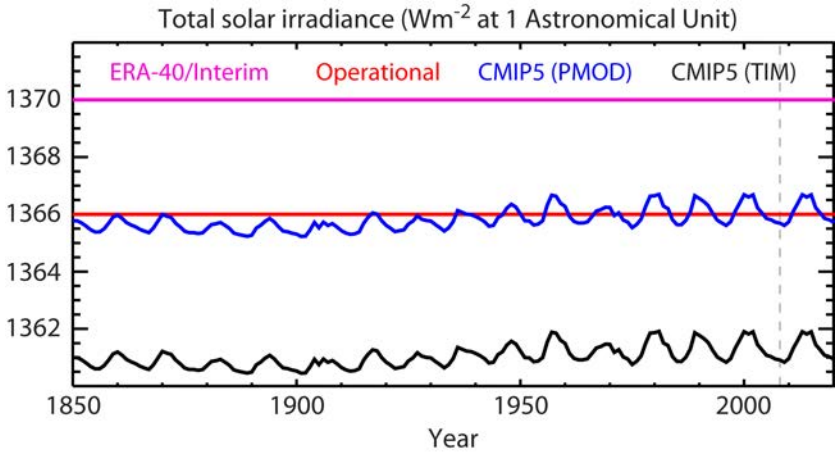

Figure 3: Total solar irradiance (Wm^{-2}) as used in ERA-40 and ERA-interim (purple), ECMWF operational model (red), CMIP5 PMOD (blue), and CMOD5 TIM (black) as used in ECMWF seasonal forecast system 4, and ERA-20CM.

ERA-40 both used 1370 Wm^{-2}.

ECMWF Seasonal System 4 does account for a variation in solar forcing. It follows the yearly-averaged TSI set from the CMIP5 recommended SPARC Solaris reconstruction (Lean *et al.*, 2005). This timeseries is based on a regression between historical sunspot and facular proxies, and recent observations (Fröhlich and Lean, 2004). As recommended by Lean *et al.* (2005), the SORCE Total Irradiance Monitor (TIM) rescaling (Kopp *et al.*, 2005) is adopted. This embodies a rescaling of a previously obtained PMOD composite with a factor 0.9965, as this insight emerged from the availability of high-quality SORCE data from 2003 onwards.

The WCRP/SPARC Solaris set contains a reconstruction from 1610 to 2008. IFS incorporates yearly TSI values from 1851. For dates after 2008, the latest solar cycle is repeated perpetually. TSI is linearly interpolated between years. The distribution of the total irradiance over the solar spectrum is not adapted, i.e., the much larger solar-cycle variations in the ultraviolet are not taken into account. Figure 3 gives an overview of the various settings. On average the PMOD scaling is in line with the choice in the operational ECMWF model. Note that the reduction of the TIM rescaling (~ 4.8 Wm^{-2}) is much bigger than the variations in the solar cycle (~ 1 Wm^{-2}). It is comparable (though opposite) to the difference between the ERA-Interim and operational configuration.

ERA-20CM uses the ECMWF Seasonal System 4 implementation, i.e., the CMIP5 recommended TIM-rescaled reconstruction.

3.2.2 Greenhouse gas concentrations

The (short-wave) radiative heating/cooling rates of the middle atmosphere strongly depend on trace gas concentrations. The most important gases are carbon dioxide (CO_2), ozone and methane (CH_4). Other relevant trace gases are nitrous oxide (N_2O), trichlorofluoromethane (CFC-11) and dichlorodifluoromethane (CFC-12). In the troposphere CO_2 acts, besides water-vapour, as the most dominant greenhouse gas.

For these quantities, the ECMWF radiation scheme uses prescribed climatological data. In IFS Cy37r3

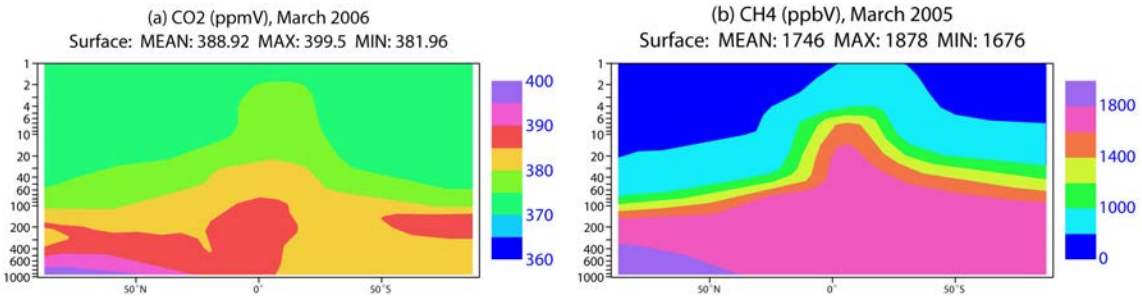

Figure 4: Vertical profile of GEMS zonal-mean CO_2 (left) and CH_4 (right) for March as used in the IFS operational configuration and ERA-20CM.

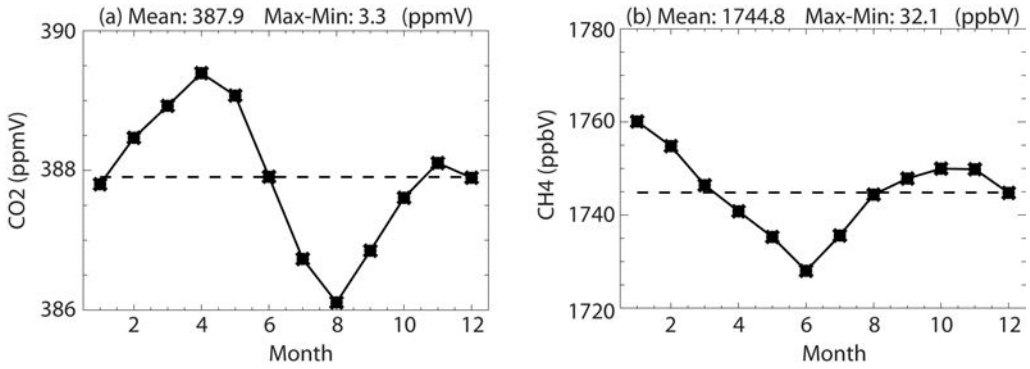

Figure 5: Monthly global mean concentrations at sea level of CO_2 (left) and CH_4 (right) GEMS reanalysis, as used in the IFS operational configuration and ERA-20CM. Months are labelled from 1 (January) to 12 (December).

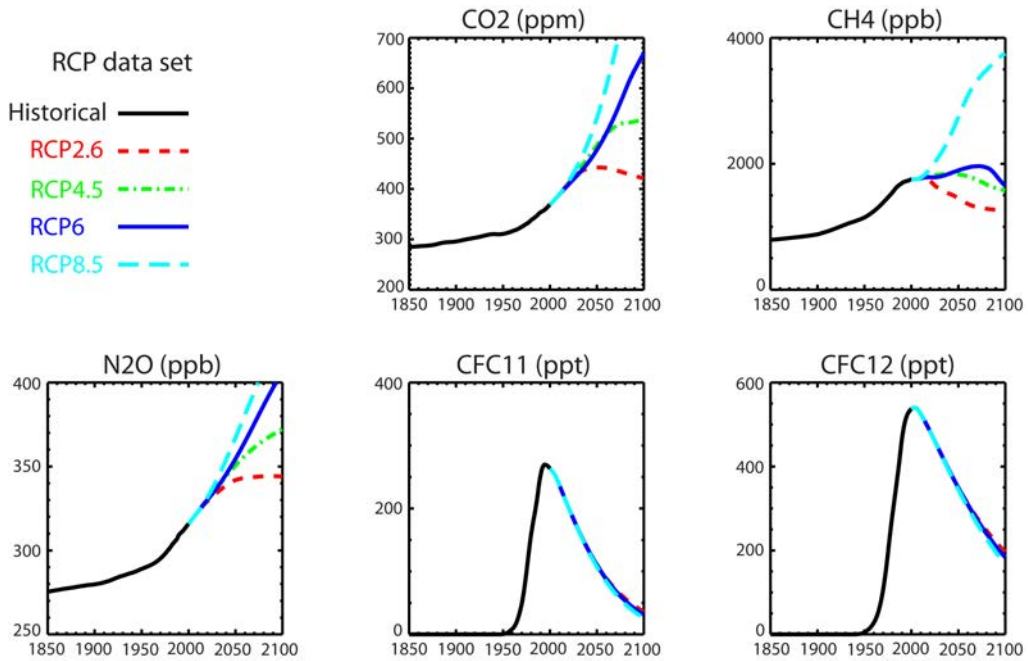

Figure 6: Long-term evolution of yearly and globally averaged greenhouse-gas concentrations at sea level as used in ERA-20CM from the CMIP5 RCP data set.

the spatial and seasonal distribution of greenhouse gases is prescribed by monthly zonally-averaged fields of volume mixing ratios. For CO_2 and CH_4 these are based on a GEMS reanalysis (Hollingsworth *et al.*, 2008) for the years 2006 and 2005, respectively, while for N_2O , CFC-11, CFC-12, CFC-22, CCL_4 climatologies from the Meteo-France transport model MOBYDIC (D. Cariolle) are used. Details may be found in Bechtold *et al.* (2009). An example of the GEMS reanalysis fields is provided in Figure 4, which displays the zonal-mean profiles of CO_2 and CH_4 for March. Although in absolute terms the zonal-mean distribution in CO_2 is reasonably homogeneous, and like-wise for CH_4 at the surface, there is a clear seasonal cycle (Figure 5).

For CO_2 , CH_4 , N_2O , CFC-11 and CFC-12, long-term evolution of greenhouse gases is described by a rescaling of the monthly-mean fields, such that the seasonal variations as displayed in Figure 5 are retained. For dates between 1850 and 2000 rescaling is based on globally averaged marine concentrations from the NASA Goddard Institute for Space Studies (GISS), and IPCC scenario A1B is followed (Pachauri and Reisinger, 2007) afterwards.

CMIP5-recommended greenhouse gas data follow the long-term evolution of Meinshausen *et al.* (2011). These include a reconstruction between 1765 and 2005 and RCP projections (RCP2.6, RCP4.5, RCP6.0 and RCP8.5) up to the year 2100. A timeseries is presented in Figure 6. For the historical period CMIP5 recommendations match the GISS data set quite well. However, recently it was realized that the IFS implementation for GISS CFC-11 is much too strong. In addition, the rescaling of CO_2 and CH_4 are based on yearly global averaged values from previously used MOBYDIC profiles, rather than on GEMS. For CO_2 this results in an overestimation of about 4.6%. This has been corrected for the ERA-20CM configuration.

ERA-20CM uses the rescaling of CO_2 , CH_4 , N_2O , CFC-11 and CFC-12 of the CMIP5 recommended RCP data set, rather than GISS. The relative distribution over season, latitude and pressure follows the standard IFS configuration.

3.2.3 Ozone concentration

The ECMWF radiation scheme uses climatological ozone concentration data. From Cy35r3 onwards this is taken from the zonally-averaged monthly-mean from the GEMS reanalysis for 2006. This comprises ozone volume mixing ratio on 64 latitudes at 91 pressure levels (998.8 hPa to 0.01 hPa). Required values are linearly interpolated according to day of the year, latitude and pressure. Besides a seasonal variation there is no long-term evolution. Details may be found at Bechtold *et al.* (2009).

The CMIP5 recommended data set is found in the AC&C/SPARC Ozone Database (Cionni *et al.*, 2011). This dataset contains monthly full three-dimensional fields for the period from 1850-2009 (historical data), and from 2010-2099 for several RCP projections. It is gridded onto 72 longitudes, 37 latitudes and 24 levels in the vertical (1000 hPa to 1 hPa). The long-term evolution of this data set is displayed in Figure 7, where the full fields have been summed to total column ozone for 4 different months and four areas.

The data set does account for variations in the solar cycle, which originate from the large variations in ultra-violet compared to those in the visible spectrum. So, although this larger variation in ultra-violet is neglected at input via the TSI (see Subsection 3.2.1), its influence is effectively included in the prescribed ozone, and in this way effectively will have an influence on the energy budget.

From the 1970s a decline of total column ozone over the Antarctic spring reflects the formation of the ozone hole. Zonal dependencies in the stratosphere appear limited, but in the troposphere there is a

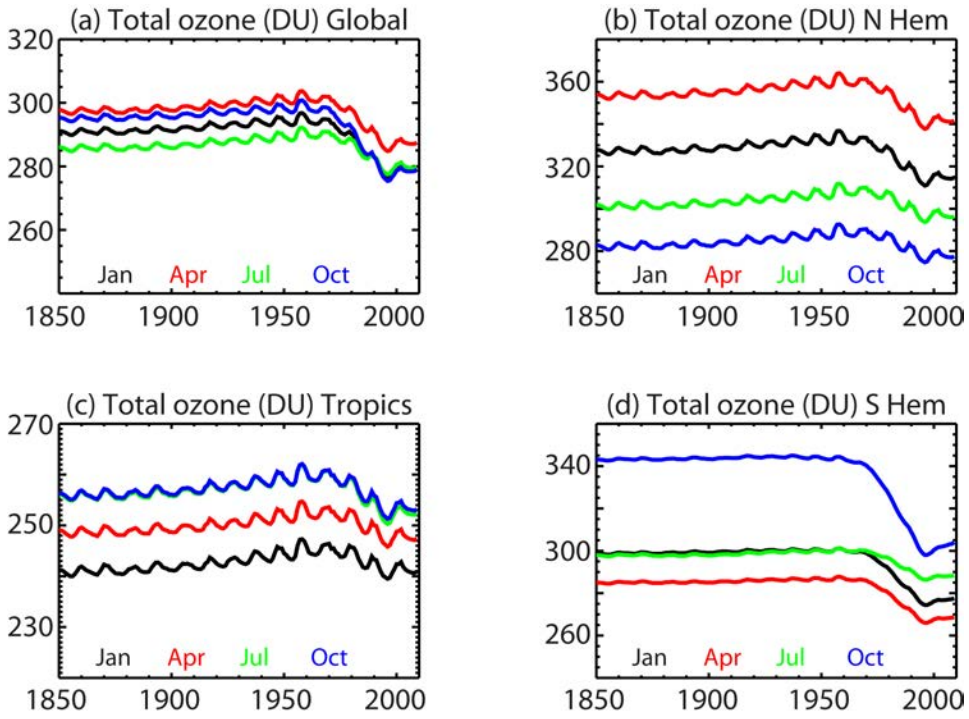

Figure 7: Long-term evolution of ozone as used in the ERA-20CM radiative forcing following the AC&C/SPARC Ozone Database. Presented are total column ozone (in Dobson, DU) obtained from a vertical integration of the full three-dimensional ozone database for the months January (black), April (red), July (green), October (blue), and averaged over the entire globe (top left), Northern Hemisphere north of 20N (top right), tropics from 20N to 20S (bottom left) and Southern Hemisphere south of 20S (bottom right).

noticeable dependency, and high values emerge over industrialised countries from the 1970's.

ERA-20CM uses the AC&C/SPARC data set throughout. Its implementation was already available in the EC-EARTH v2.2 configuration. The part of the code that handles this ingestion has not evolved much in time, and was successfully merged into the ERA-20CM configuration. Ozone concentration is linearly interpolated to the actual date, latitude, longitude and pressure. Projections based on RCP2.6, RCP4.5 and RCP8.5 have been included.

3.2.4 Tropospheric aerosols (optical depth)

The presence of aerosols blocks incoming (short-wave) radiation. The amount is characterized by the optical depth, which linearly relates to the aerosol sun-ward mass per unit area (called burden or load). The extinction factor, which expresses this relation depends on particle size and shape, radiation wave length, and for some aerosols humidity.

In the standard version of IFS the effect of aerosols on radiative transfer is based on prescribed climatological distributions of optical depth from sea salt, soil/dust, organic, black carbon and sulphate (SO_4). Input are monthly-mean geographical fields for optical depth at the surface from Tegen *et al.* (1997). The optical depth per vertical model layer is determined under the assumption of an empirical vertical profile following Geleyn, such that the total optical depth equals the Tegen *et al.* (1997) surface values. Organic and sulphate aerosols are grouped together in a continental class. For this class a uniform background

Surface class	Aerosol Type	Vertical profile	Background profile
Continental	Organic + Sulphate	$(p/p_s)^R$	$0.03\ \Delta p/(p_s - p_t)$
Maritime	Sea Salt	$(p/ps)^R$	none
Desert	Soil/Dust	$(p/ps)^{R/3}$	none
Urban	Black Carbon	$(p/ps)^R$	none

Table 2: Grouping of tropospheric aerosols in IFS. p is pressure, $p_s = 1013.25$ hPa, $p_t = 193.3$ hPa is surface pressure and tropopause pressure for a standard atmosphere, respectively, and R=8.434

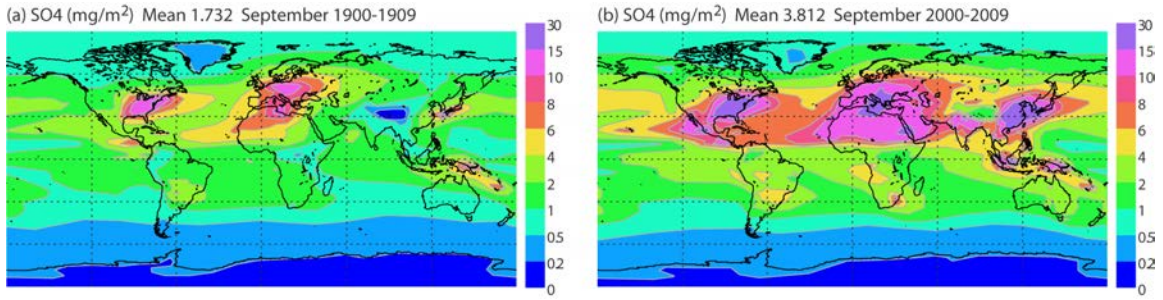

Figure 8: Total burden (10^{-6} kg m^{-2}) in September for sulphate from the CMA3.5 simulation for the period 1900-1910 (left) and 2000-2009 (right), respectively.

distribution is added, with a total optical depth of 0.03. The vertical extent of soil/dust (desert class) is deeper than it is for the other aerosol types. An overview is given in Table 2. All distributions are confined to the troposphere, i.e., any resulting values above the tropopause are cut off. The climatological data set is valid for 550 nm. For other wave lengths, IFS remaps optical depth based on estimates of the frequency-dependency of extinction coefficients (Hess *et al.*, 1998).

The largest contribution to optical depth is formed by soil/dust, sulphate and organic aerosols. They display a significant seasonal and local variability. From July to September optical depth for soil/dust reaches values above 1.0 in Saudi Arabia, which is much higher than the global average of about 0.03. Sulphate peaks at around 0.3 in summer over industrialised areas in the Northern Hemisphere. Besides these seasonal and geographical variations, IFS does not account for a long-term evolution.

CMIP5 recommended aerosol data embrace simulations based on the NCAR Community Atmospheric Model CAM3.5 and using a bulk aerosol model driven by CCSM3 (CMIP4) SST. For historical data, sources were the 1850-2009 IPCC emissions (Lamarque *et al.*, 2010), while projections (2010-2100) follow RCP emissions (van Vuuren *et al.*, 2011). Monthly 10-year averages are available on full three-dimensional fields of 96 latitudes, 144 longitudes, and 26 sigma levels in the vertical.

For ERA-20CM, only recommendations for sulphate were considered, since it accounts for the largest anthropogenic contribution to aerosols. The long-term variation of other aerosols was not taken into account.

For sulphate the CMIP5 data indicate a huge increase in levels during the 20th century, with a maximum around the 1980s. Concentrations are currently easing (with the exception of East Asia) and all RCPs assume a steady decrease during the 21st century. An illustration is provided in Figure 8 which displays the vertical integration to total burden for the September 1900-1910 (left) and 2000-2009 (right) average, respectively.

In IFS the climatological aerosol fields are imported as total optical depth at the surface for 550 nm. The

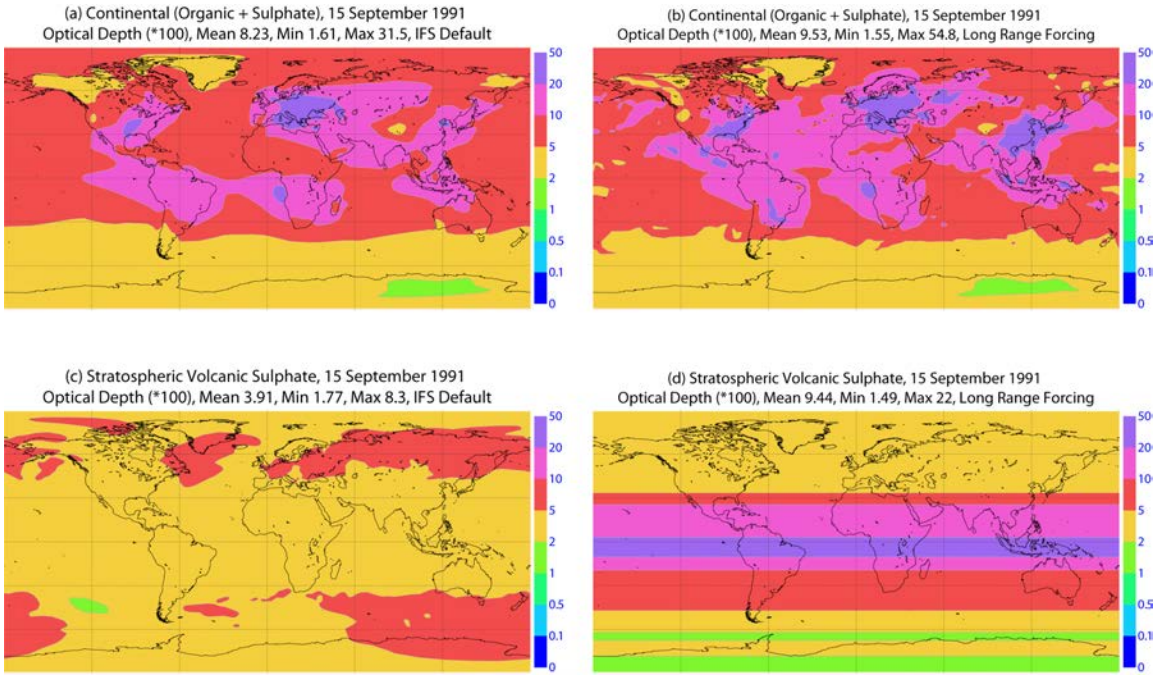

Figure 9: Total optical depth for organic and sulphate (top) and volcanic sulphate (bottom) for the default configuration of IFS (left) and the long-range CMIP5 options as used in ERA-20CM (right) for 15 September 1991.

CAM3.5 data set, however, provides three-dimensional fields of sulphate concentrations (in μgm^{-3}). A minimal, conservative approach was followed. Rather than retaining the full information, the total burden is summed over the vertical. A linear interpolation to month and decade of the resulting two-dimensional fields is performed. The sulphate content per layer in the vertical is then determined following the above-described vertical redistribution, and converted into partial optical depth using the IFS humidity-dependent extinction factors for 550 nm. Conversion to other wave lengths is again based on the method of (Hess *et al.*, 1998). An example of the two climatologies is displayed in panels (a, b) of Figure 9. It shows the total optical depth for the continental class (organic plus sulphate) on the model radiation grid for 15 September 1991, i.e., after interpolation to year and month, regridding, and summing over all levels in the vertical. Although the general patterns between Tegen *et al.* (1997) (left) and CMIP5 (right) are similar, CMIP5 is slightly stronger, especially over East Asia and the Atlantic. The low values south of -40S represent the background of 0.03 (see Table 2).

3.2.5 Stratospheric aerosols (optical depth)

In the stratosphere, aerosols mainly have a volcanic origin. For many volcanic eruptions the plume does not reach the stratosphere. When it does, such as Pinatubo in 1991, volcanic sulphate can remain in the stratosphere for many months, where it mixes within large predominantly zonal bands. Volcanic ash has a shorter life time. In the troposphere volcanic aerosols are washed out reasonably quickly by precipitation. The operational configuration of IFS Cy37r3 does not account for the evolution of stratospheric aerosols. It uses a standard average background optical thickness of 0.045 for sulphate according to Tanre *et al.* (1984), and ignores contributions from volcanic ash. The background value is evenly distributed over the stratosphere, assuming a constant volume-mixing ratio.

The CMIP5 recommended data set for volcanic aerosols uses a GISS reconstruction by Sato (as described

Class	Standard IFS	ERA-20CM	Vertical profile
Volcanic Ash	nil	0.007	$\Delta p/p_t$
Volcanic Sulphate	0.045	GISS	$\Delta p/p_t$

Table 3: Grouping of stratospheric aerosols in IFS; background profiles are based on Tanre et al. (1984). p is pressure and $p_t = 193.3$ hPa is the tropopause pressure for a standard atmosphere.

at http://data.giss.nasa.gov/modelforce/strataer/). As emerges from Sato *et al.* (1993), historical reconstruction of volcanic stratospheric sulphate is non-trivial. The data set contains monthly zonal-mean estimates from 1850 to current date of optical depth stratified into 24 latitude bands and four 5 km-thick layers from 15 km, 20 km, 25 km and 30 km height, upwards.

IFS does provide an option to incorporate the GISS data set. For this, the four vertical optical depths are summed together, and then redistributed over the stratosphere assuming a constant mixing ratio. It replaces the background value of 0.045. In addition, this option adds a background for volcanic ash of 0.007, according to Tanre *et al.* (1984).

ERA-20CM uses the GISS data set for volcanic aerosols, in combination with a constant background for volcanic ash. The original IFS implementation, which accounts for the years 1957 to 2000, was extended back to 1850. After 2000, volcanic sulphate is assumed to be zero. Recently, a new version of the GISS data set has become available which also includes the years 2000 to 2012. This extension was not taken into account, and fortunately in this decade, no eruptions occurred that significantly affected the stratosphere.

The evolution of total optical depth from GISS, as used in the ERA20-CM configuration is displayed in Figure 10. It clearly shows the mayor eruptions over the last 160 years. For Pinatubo, the effect on total optical depth is presented in panels (c, d) of Figure 9, which displays the geographical distribution of 15 September 1991, three months after its eruption. Panel (c) displays the background profile of (Tanre *et al.*, 1984) as used in the operational configuration of Cy37r3. The reason why it is not exactly 0.03 everywhere is that the density is based on a climatological stratospheric thickness of 193.3hPa, while the extent itself starts at the model tropopause, which varies. Panel (d) clearly displays the much enhanced levels from Pinatubo, distributed into perfectly-mixed latitude bands.

3.3 ECMWF formulation of (land) surface parametrization

In IFS, the surface scheme is based on the Hydrology Tiled ECMWF Scheme for Surface Exchanges over Land model (HTESSEL, Balsamo *et al.* (2008)). Each model grid point can consist of a number of subgrid tiles, for which surface fluxes are calculated separately. Land tiles are determined by climatological distributions for low and high vegetation and their cover from the 2'30" Global Land Cover Characteristics (GLCC, Loveland *et al.* (2000)). Neither seasonal variation nor a long-term evolution is taken into account. Snow and sea ice tile allocation follow the prognostic model state, so these do allow for variations.

For land tiles surface fluxes depend on the leaf area index (LAI). From IFS Cy36r4 onwards LAI is based on MODIS data, rather than diagnostically from vegetation type (Boussetta *et al.*, 2011). This climatology is varying monthly, and therefore allows for seasonal effects in vegetation.

In the McRad scheme reflection of short-wave radiation at the surface distinguishes between direct and diffuse radiation, and between UV-visible (200 - 700 nm) and near-infrared (700 - 5,000 nm). The resulting four surface albedos are based on monthly-mean climatologies from MODIS albedo over the

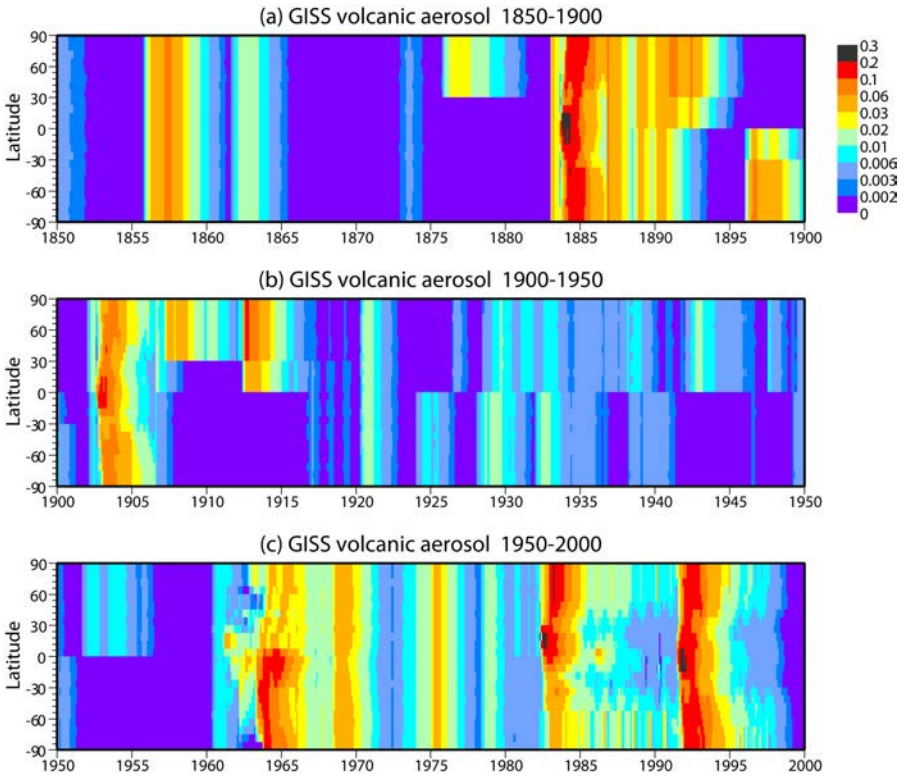

Figure 10: Long-term evolution of optical depth at 550nm for stratospheric volcanic sulphate as used in ERA-20CM from the April 2002 version of GISS (http://data.giss.nasa.gov/modelforce/strataer/). Mayor eruptions over the last 160 years are clearly visible, such as Cotopaxi in 1855, Krakatau in 1883, Santa María in 1902, Novarupta in 1912, Agung in 1963, Fernandina in 1968, El Chichón in 1982 and Pinatubo in 1991.

year 2000-2003 (Schaaf *et al.*, 2002). Over water, ice and snow, the climatological albedo is adapted according to available prognostic model information.

For CMIP5 the Land-use Harmonization (LUH) team has prepared a set of land-use scenarios that smoothly connect historical reconstructions of land-use, based on HYDE data and national wood harvest statistics, with future projections of land use based on the Integrated Assessment Model (IAM) implementations of RCPs. Fractional land-use patterns and underlying land-use transitions are provided annually for the time period 1500-2100 at $0.5^o \times 0.5^o$ resolution.

The EC-EARTH consortium has merged the LUH data set with the GLCC database to provide decadal T159 fields for vegetation type and cover. For recent decades locally large differences are found with the climatologies as used in IFS. For example, the EC-EARTH construction does not distinguish between un-irrigated crops and irrigated crops. A visual evolution of the decadal maps do not reveal a dramatic large-scale evolution over the 20th century.

No long-term evolution was available for LAI, nor for the distinction between direct and diffuse albedo. Since only limited information from CMIP5 recommendations could, in principle, be incorporated in the ECMWF surface parametrization, it was decided not to use any. The ERA-20CM surface parametrization thus follows the operational setting of IFS as described above.

Net flux	TKF09	Cy37r3	CMIP5	Solar	GHG	O_3	Trop S	Volc S	SST
TOA SW radiation	**239.4**	**238.3**	0.45	-0.81	0.00	0.02	0.14	1.09	0.17
TOA LW radiation	**-238.5**	**-240.8**	-0.52	0.14	-0.29	0.18	-0.05	-0.41	0.30
TOA total (R_T)	**0.9**	**-2.5**	**-2.6**	**-3.2**	**-2.8**	**-2.3**	**-2.4**	**-1.8**	**-2.0**
Surface SW radiation	**161.2**	**161.3**	-0.36	-0.55	0.04	-0.05	-0.29	0.50	0.47
Surface LW radiation	**-63**	**-59.4**	-0.12	-0.03	-0.22	0.13	-0.07	0.00	-0.62
Surface sensible heat	**-17**	**-18.8**	0.10	0.00	-0.00	-0.02	0.16	0.00	-0.21
Surface latent heat	**-80.0**	**-83.6**	0.22	-0.15	-0.12	0.12	0.24	0.13	0.69
Surface total (S_F)	**0.9**	**-0.5**	**-0.7**	**-1.2**	**-0.8**	**-0.3**	**-0.5**	**0.1**	**-0.2**
Total input $R_T - S_F$	**0**	**-2.0**	**-1.9**	**-1.9**	**-2.0**	**-2.0**	**-1.9**	**-1.9**	**-1.9**

*Table 4: Annual mean global radiation budgets ($Wm^{-2}$and positive downwards), as estimated for the period March 2000 to May 2004 by Trenberth et al. (2009) (*TKF09 *), and accumulated for the period September 2000 to August 2001 for the 13-months 4-member T159 AMIP runs based on standard IFS Cy37r3 forcing (Cy37r3), CMIP5 forcing (CMIP5), CMIP5 solar only (Solar), Greenhouse gases only (GHG), ozone only (O_3), tropospheric sulphate only (Trop S), volcanic sulphate only (Volc S), and HadISST2.0.0.0 only (SST), respectively. Numbers in bold represent actual values, while non-bold numbers are relative to the Cy37r3 control run.*

3.4 Energy budget sensitivity with respect to CMIP5 forcing

Although a model integration without any data assimilation is not able to represent the evolution of the atmosphere on a synoptic level, it should be able to exhibit a realistic average model state. At ECMWF this property is regularly tested in a standardized fashion. For this, a 4-member AMIP ensemble is integrated for a 13-month period from the beginning of August 2000. Starting point is ERA-Interim for four initial dates each separated by 18 hours. All runs are bounded by analysis SST and SIC, and total mass is fixed. The first month is later discarded. The AMIP members are compared with GPCP, TRMM, SSMI, ERBE and CIRES data sets and with ERA-Interim, using a quick-run diagnostic package.

This environment is here used to assess the average behaviour of standard Cy37r3, the CMIP5 configuration, and its various components, as described in sections 3.1 and 3.2. In total 8 configurations were explored. The two basic configurations are T159 using the default Cy37r3 setting and Cy37r3 using the CMIP5 forcing terms for solar irradiance, greenhouse gases, ozone and aerosols (troposphere and stratosphere) all together. Another five AMIP runs were conducted where only one specific CMIP5 forcing term is included, while an 8th experiment is based on default Cy37r3, but with SST and SIC forcing from (realization 103 of) HadISST2.0.0.0. Note that the results as obtained from these runs apply to the year 2000-2001, i.e., a year where the CMIP5 forcing does not differ too much from the default IFS setting.

In order for ERA-20CM to be in quasi-equilibrium, energy budgets must balance. The total amount of net incoming energy at the top of the atmosphere (TOA) should be approximately equal to the net amount leaving the atmosphere at the surface. This was tested for the 8 runs. Average global net energy budgets are presented in Table 4 and compared to budgets as estimated by Trenberth *et al.* (2009), to be denoted by *TKF09* , hereafter. For these experiments, the individual net terms of TOA radiation, surface radiation, and latent and sensible heat agree with *TKF09* within a few Wm^{-2}. This is, given the low model resolution, quite a good result. The total sums of the budgets at the TOA and surface, however, do not agree and in addition have the wrong sign. Based on the observed climate trend over the past decades, *TKF09* estimate a net gain (R_T) at the TOA of 0.9 Wm^{-2}, which is passed through the atmosphere, and is subsequently absorbed by the (ocean) surface. The T159 runs all exhibit an energy loss at the TOA, ranging between -2.0 and -3.2 Wm^{-2}. In addition, for all but one configuration, energy is extracted from the surface, rather than inserted into the surface. This would indicate a cooling of the

ocean, rather than warming. In the context of an AMIP run, this has no consequences, since the ocean surface is prescribed, regardless of the model fluxes. A similar incorrect net energy flow was observed by Magnusson *et al.* (2012) in a coupled ocean-atmosphere integration where the SST was strongly constrained to observations. An integration where SST was not constrained did agree well with the estimate of *TKF09* of a net energy flux into the surface, and Magnusson *et al.* (2012) concluded that the incorrect sign in their strongly constrained integration was induced by a systematic difference between the SST model climate and observed climate.

The net total energy input (TEI), being the difference between R_T and the net surface flux (S_F) is negative as well, and close to $-2\,\mathrm{Wm}^{-2}$ for all 8 AMIP runs. In principle this value should be very close to zero, like *TKF09* , since this represent the net energy flux into the atmosphere. However, the average of one year only may allow for some deviation, since due to inter-annual variations, the relative large seasonal net fluxes cannot be expected to balance exactly in one year. This will be further elaborated on in Section 5, where the evolution of the ERA-20CM energy budget over the entire 20th century is discussed. A sensitivity ensemble for which dry mass is conserved (like ERA-20CM) rather than total mass only indicates a minor effect on the TEI (not shown). Larger imbalances have been found for ERA-40 and ERA-Interim (Berrisford *et al.*, 2011b), but these involve data assimilation where the ingestion of data introduces small discontinuous steps between the analysis and its previous forecast. In addition, part of diagnostic imbalances may actually represent spin-up effects in the short forecast from the analyses, from which the budgets are usually extracted.

Although the net budget, TEI, is non-zero, its value is quite robust between the various experiments. For instance, the CMIP5 recommended TIM reduction in solar irradiance by 0.35%, leads not only to this reduction in the TOA solar incident radiation, but also to a similar reduction in the TOA net solar radiation ($-0.81\,\mathrm{Wm}^{-2}$) and reflected solar radiation at the surface ($-0.55\,\mathrm{Wm}^{-2}$). As a reaction to the reduced solar energy input, the atmosphere slightly cools (the global average two-metre temperature cools by 0.05 K). This leads to a slight reduction of thermal radiation into space and the surface ($0.14\,\mathrm{Wm}^{-2}$ and $-0.55\,\mathrm{Wm}^{-2}$, respectively) and a slight change in sensible and latent heat, such that the TEI remains nearly unchanged ($-1.9\,\mathrm{Wm}^{-2}$). In other words, the model readjusts such that an initial energy imbalance is counterbalanced.

Table 4 shows a relative large increase in the TOA solar radiation for volcanic sulphate, although the GISS optical depth is basically zero for the 2000-2001 period. The reason for the increase is the omission of the perpetual background value of 0.03 in the default IFS configuration, as e.g., displayed in panel (c) of Figure 9. The change of $1.09\,\mathrm{Wm}^{-2}$ with respect to a small change in stratospheric optical depth (0.03) indicates a sensitive model behaviour with respect to volcanic aerosols. Note that the net effect on TEI is again almost unaltered ($-1.9\,\mathrm{Wm}^{-2}$).

4 Production and archiving

The ERA-20CM ten-member ensemble was conducted in an environment that is used at ECMWF to make long forecast integrations. The ensemble creates a huge amount of forecast data, and to manage this, the century-long run was split into yearly chunks. The first initial state for 31 December 1898 was taken from the ERA-Interim analysis of 31 December 1988. The first forecast step is valid for 00 UTC January 1 1899. The year 1899 is to be considered as spin-up of the random draw of the initial state from present-day climatology towards a state representative for the end of the 19th century. This especially concerns prognostic ozone and to a lesser extent the initial state of the other model quantities with respect to a one-degree too warm ocean surface and out-of-date radiative forcing. The initialization

of subsequent years was obtained from the exact (binary) final state of the previous year, including all model tendencies. This prevents spin-up effects at the first of each January, and the result is perfectly seamless as if the century-long run were integrated in one go. The ensemble was integrated until 21 UTC 31 December 2009.

The analysis step that is required for the ingestion of HadISST2.0.0.0 (see Section 3.1.2), was performed beforehand in a separate dedicated environment. The allocation between HadISST2 realization and ERA-20CM ensemble member is displayed in Table 1. The resulting T159 SST and SIC GRIB fields were read in as boundary conditions along with a number of other external fields, such as albedo, LAI and vegetation type and cover. The setup of the CMIP5 forcing was invoked by the optional switches in Cy37r3 as discussed in Section 3.

The MARS archive is organized with respect to a number of keys. These include class, stream, date, time, step, level and parameter. For ERA-20CM a special class=em was created to allow for the distinction from operational data (class=od), ERA-Interim (class=ei), etc. Output was generated for each 3h interval, i.e., for 00 UTC, 03 UTC, etc. to 21 UTC for each day. Only a limited number of quantities was actually archived for each step (stream=enda). For the majority of model fields at the various levels, only monthly means have been archived. This involves both monthly fields averaged for a specific synoptic time (stream=edmm) and monthly means over all 8 daily values (stream=edmo). The archive encompasses surface fields, upper air fields at all 91 model levels, 37 pressure levels, 16 levels for potential temperature, and the 2000 level for potential vorticity for a limited set of parameters, and has a total size of about 35 terabytes. The full list of monthly mean fields is very similar to the list of ERA-Interim (Berrisford *et al.*, 2011a). Unfortunately no data is available for ocean-wave parameters. Date and time relate to the actual date and time of the forecast, rather than to the initial state (31 December 1898) plus forecast step. This latter, usual convention, would be extremely cumbersome for the century-long integration, and besides, appeared technically impractical. For each date and 8 times there are only two forecast steps: step=0 related to instantaneous fields such as temperature and pressure, and step=3 relating to accumulative fields such as surface stress or TOA net solar radiation.

The ERA-20CM archive is accessible from the ECMWF data server (apps.ecmwf.int/datasets/).

5 Long-term evolution of energy budgets

As illustrated in Subsection 3.4, a small change in boundary conditions will induce a small though persistent readjustment in energy budgets, which leads to a slightly shifted, new model climate. Figure 11 provides an overview of the evolution of energy budgets for the ERA-20CM ensemble. Presented are one-year averages, which were obtained from the monthly-mean fields in the MARS archive. The inter-annual variability of these yearly-averaged energy budgets is much smaller than the amplitude of the seasonal cycle (typically around 5 Wm^{-2}, not shown). The difference between members (light colours) and ensemble mean (dark colours) is small (typically below 0.5 Wm^{-2}), i.e., the total budgets are rather robust, and do not really depend much on the details of the underlying synoptic situation. This is also true for the monthly averages (not shown).

In line with the one-year test integrations that were presented in Subsection 3.4, the T159 model in general displays a net outflux of energy into space (about 0-2 Wm^{-2}), and a net influx at the surface (about 0.5-2.5 Wm^{-2}). This is opposite to what is expected for a situation of global warming. The observed global average SST is stable between 1940 and 1970, as is e.g. apparent from panel (a) of Figure 1 for HadISST2. For that era both the total net flux at the TOA and the surface should approximately vanish. For ERA-20CM this is obviously not the case; the TOA total net flux ($\mathbf{R_T}$) is about 1.5 Wm^{-2}too low,

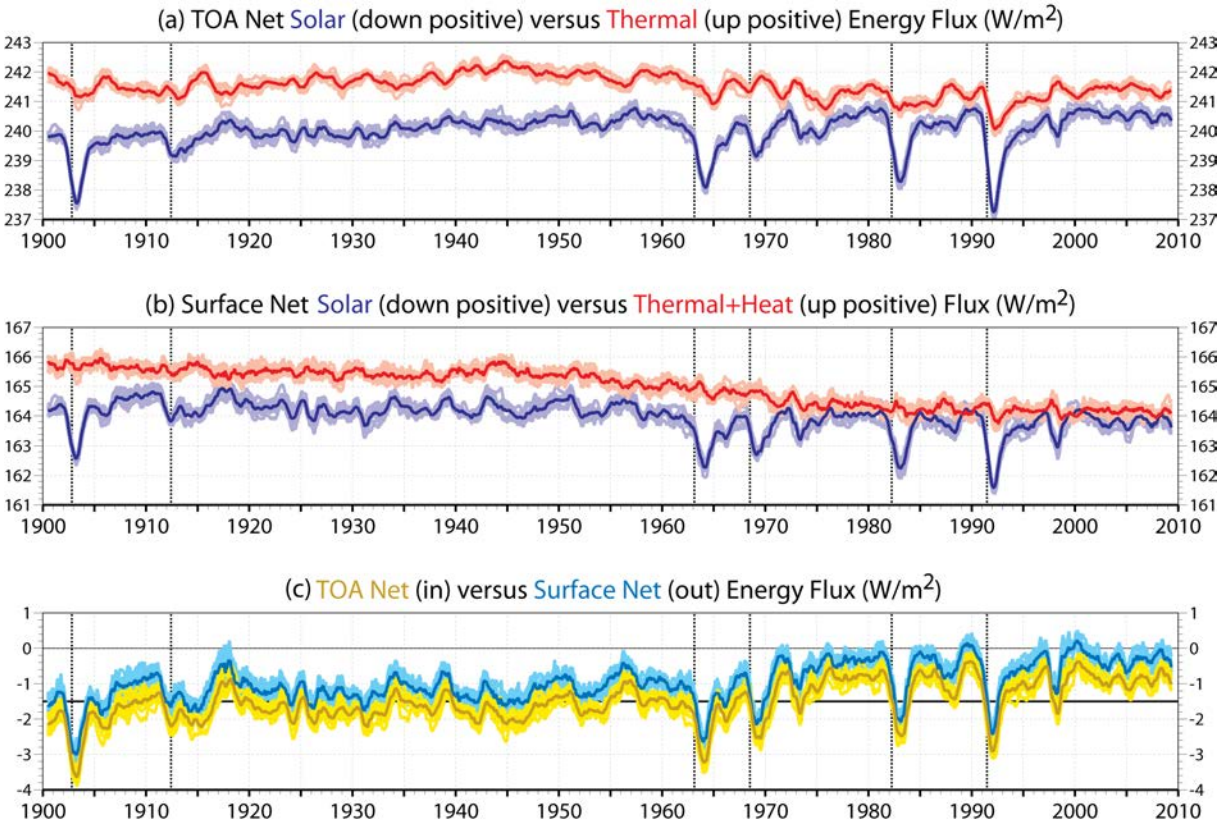

Figure 11: Evolution of the one-year moving average of energy budgets in ERA-20CM for (panel a) TOA net solar radiation (blue, downward positive) and TOA net thermal radiation (red, upward positive), (panel b) surface net solar radiation (blue, downward positive) and the sum of surface net upward thermal radiation, latent heat and sensible heat (red, upward positive), and (panel c) TOA net total radiation ($\mathbf{R_T}$, gold, downward positive) and surface net total radiation ($\mathbf{S_F}$, blue, downward positive). Dark colours represent the ensemble mean, light colours the individual ERA-20CM members. The vertical black solid lines indicate the eruption dates (in chronological order) of Santa Maria, Novarupta, Mount Agung, Fernandina Island, El Chichón, and Pinatubo.

and the surface total net flux ($\mathbf{S_F}$) is about 1 Wm^{-2}too low.

Again, this incorrect direction of energy flows does not have a big influence on the ERA-20CM ensemble, since any effect on the ocean is overruled by the prescribed SST and SIC. In coupled mode the model would cool both the SST and surface temperature, but in the ERA-20CM uncoupled mode the prescribed increasing SST actually leads to an increase in global surface temperature, rather than a decrease.

On the other hand, the total net input in the atmosphere ($\mathbf{R_T} - \mathbf{S_F}$) should balance to zero, since any non-zero value would lead to a change in total atmospheric energy. Instead, a quite robust value of about -0.5 $\mathrm{Wm}^{-2}$is found. The atmosphere energy content is much lower than that of the ocean, and according to an estimate of 2623 MJm^{-2} (Berrisford *et al.*, 2011b), a deficit of 0.5 Wm^{-2}would lead to a loss of energy of 0.6% per year. Such a change is not observed in the AMIP runs. In fact, the ERA-20CM members actually gain total energy by about 0.6% over the entire length of the century (not shown). Apparently, there are some small hidden energy gains in the model which are not incorporated into the book keeping of the energy budgets, such that an apparent net outflux of 0.5 Wm^{-2}actually represents a quasi-stationary atmosphere. Possible sources include the fixing of the dry mass, or some inconsistencies

in the model advection scheme or model physics.

After 1970, when the global average SST starts rising, the net surface and TOA fluxes become around 1 Wm^{-2}less negative. So although the overall sign is incorrect, the direction and magnitude of the trend is correct. Compared to the offset of -1.5 $Wm^{-2}$and -1 Wm^{-2}, an evolving downward flux into the ocean emerges from 0 to about 1 Wm^{-2}, as estimated by *TKF09* .

The evolution of the imposed total solar irradiance (TSI) is reflected in the TOA incident solar radiation (not shown), which is four times smaller than the TSI (due to the ratio between the Earth's cross section and surface area). The amplitude of the solar cycle of a few tenths of a $Wm^{-2}$is too small to stand out in the evolution of the TOA net solar radiation (panel a, red curve).

The effect of volcanic eruptions on the net solar radiation is very clear. For all major eruptions during the 20th century (indicated by the solid vertical lines), a sharp dip up to several $Wm^{-2}$is observed at the TOA, which is the result of an increased reflection and absorption by stratospheric aerosols. Reflection at the surface is reduced as well, because less sunlight reaches the surface. These dips are followed by a much weaker response in net thermal radiation (TOA and surface). As a result net downward fluxes decrease and have a small temporary effect on the average global surface temperature.

At the surface the sum of net thermal radiation and heat fluxes shows a decrease by around 2 Wm^{-2}in magnitude over the 20th century, especially building up after 1970 (panel (b) of Figure 11). At first sight this seems counter-intuitive, since global warming would suggest an increase in thermal radiation. However, the global average 2m temperature rises faster than SST, as illustrated later in Figure 20. The ocean is on average slightly warmer than the air above it, and, therefore the difference between the two, which relates to the net surface flux, diminishes. The increase in downward thermal radiation (about 6 Wm^{-2}) outweighs the smaller increase in upward thermal radiation (about 4 Wm^{-2}). The sensible heat flux decreases by about 0.4 Wm^{-2}in magnitude (reduced temperature difference), and the latent heat flux increases by about 0.6 Wm^{-2}in magnitude (more evaporation), which all adds up to a reduction of about 2 Wm^{-2}in the total magnitude of the thermal net radiation plus heat fluxes at the Earth's surface.

6 Upper-air model climatology and long-term trend

The zonal-mean model climate for tropospheric and stratospheric temperature, zonal wind and humidity is presented in panels (a), (c) and (e) of Figure 12, respectively. Contours show the ensemble mean, averaged over the first decade of the 21st century. Colours indicate the average difference from ERA-Interim, which (aside near the top of the stratosphere and to some degree humidity elsewhere in the stratosphere in particular) can be regarded as a proxy for the actual ten-year climate. Similar plots for the last two decades in the 20th century show consistent patterns, and the ensemble spread within the ten-year averages are typically within 1 K, 1.5 $m\,s^{-1}$ and 5% for temperature, wind and humidity, respectively (not shown). Hence, most patterns are statistically significant and rigid over time.

In general the circulation is correct, especially in the lower half of the atmosphere. Above 500 hPa there are some clear biases with respect to ERA-Interim. The free ERA-20CM model has a cold bias around the tropopause, which is accompanied by a dry bias in the upper troposphere and lower stratosphere (panel (e)). This bias is known to be reduced at higher model resolution. The upper part of the stratosphere displays a warm bias, which is largest for the Southern Hemispheric winter (not shown). The strength of the jet cores is slightly overestimated. Larger biases are found in the stratosphere, which are known to be sensitive to the model vertical diffusion. The overestimation in the polar stratosphere mainly occurs during winter (not shown). The bias in the tropical stratosphere is partly related to the quasi-biennial

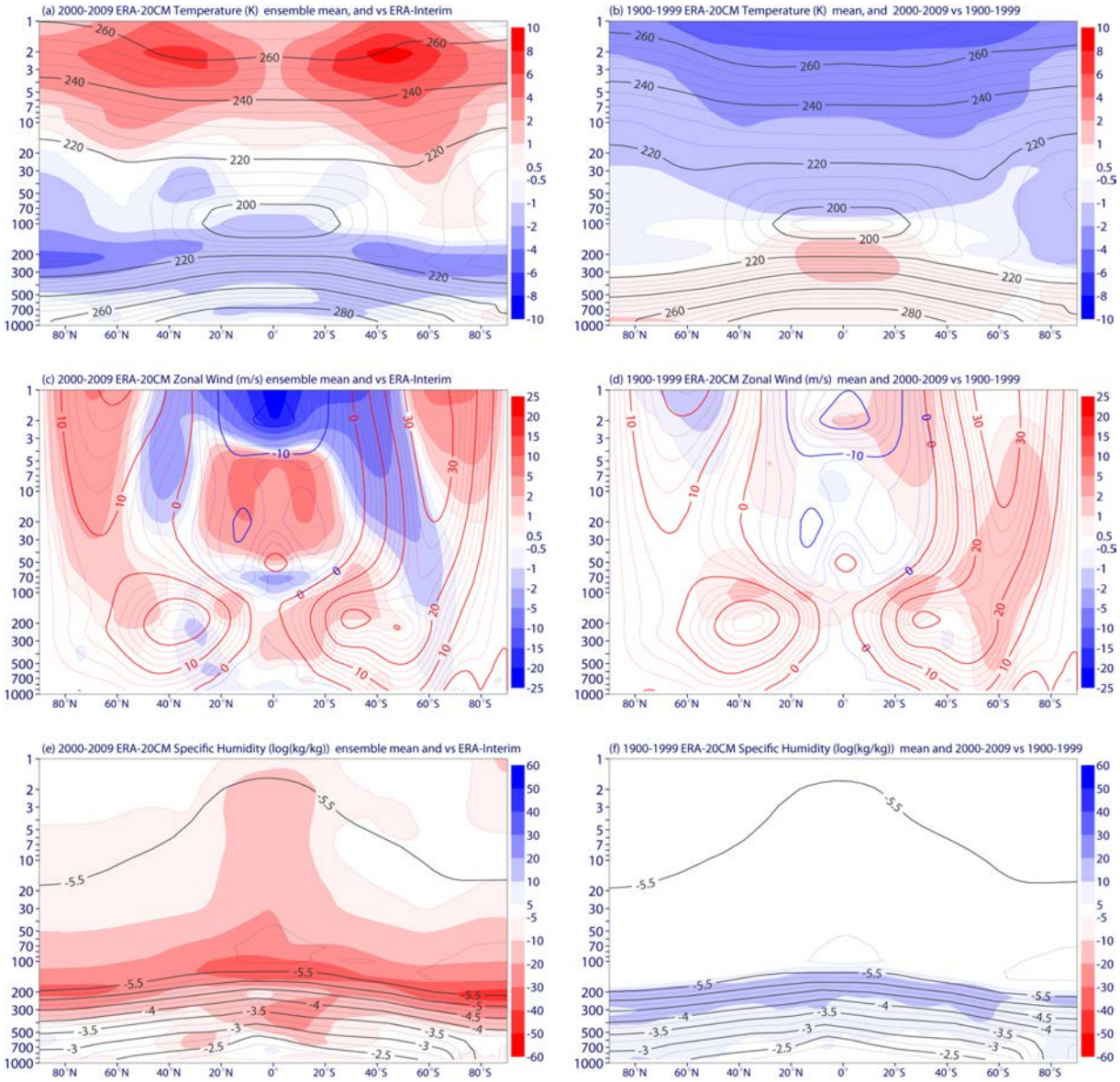

Figure 12: 2000 to 2009 ERA-20CM ensemble mean (contours), its difference with ERA-Interim (colours), 1900-1999 ERA-20CM ensemble mean and the 2000 to 2009 trend (colours) for left and right panels, respectively, for temperature (panels a, b), zonal wind (panels c, d) and specific humidity (panels e, f). For humidity, contours represent the $\log_{10}$ *of mass mixing ratio, while the colours show the relative difference in percent.*

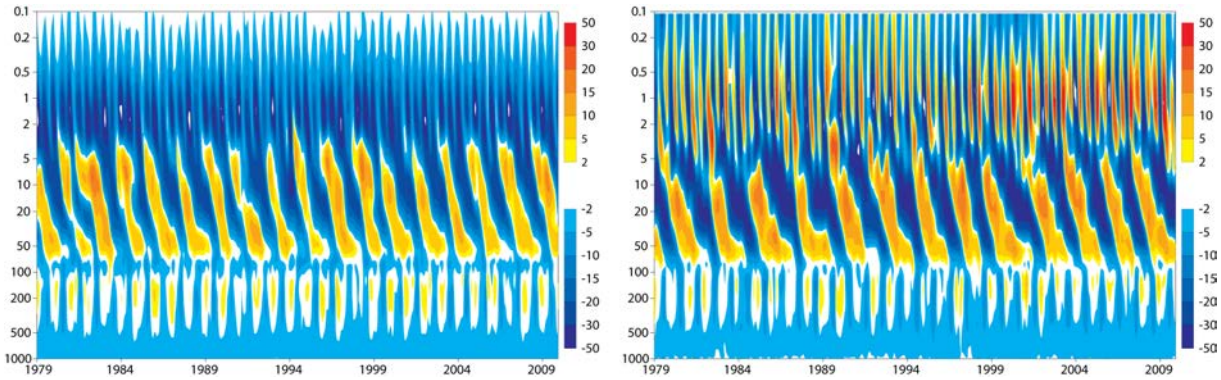

Figure 13: Monthly mean eastward wind averaged over 5S-5N for 1979-2009 in (left) ERA-20CM, ensemble member 0, and (right) ERA-Interim. The data are temporally and spatially averaged on model levels but plotted with a logarithmic pressure scale by assuming a surface pressure of 1013.25 hPa.

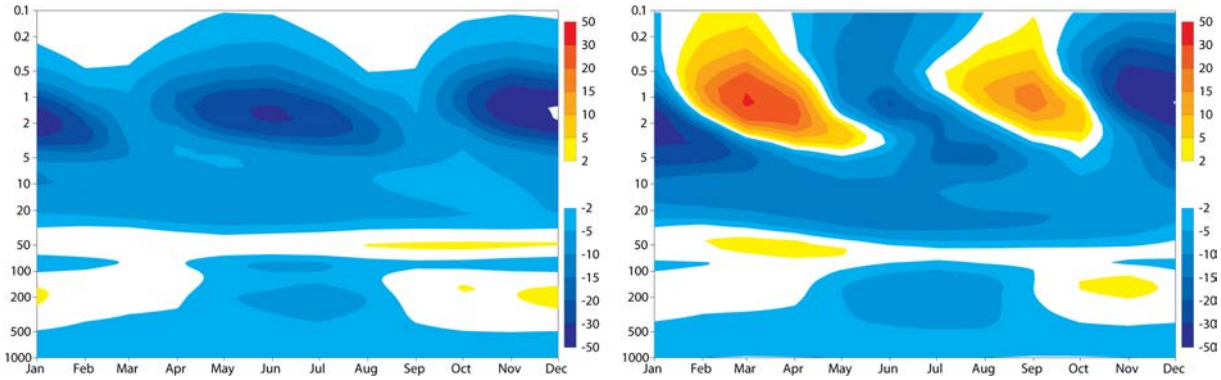

Figure 14: Climatological monthly mean (mean annual cycle) eastward wind averaged over 5S-5N for 1979-2009 in (left) ERA-20CM, ensemble member 0, and (right) ERA-Interim. The data are temporally and spatially averaged on model levels but plotted with a logarithmic pressure scale by assuming a surface pressure of 1013.25 hPa.

oscillation (QBO) and semi-annual oscillation (SAO).

The representations of the QBO and SAO in the IFS depend on several aspects of the model formulation in the tropical region including resolved large-scale and gravity waves and the parameterisation of the subtle effects of gravity waves on the momentum budget. Hence, the representations of the QBO and SAO vary with model release and resolution. The QBO in ERA-20CM has a period of about 1.8 years (Figure 13, panel (a)) which is shorter than the period of 2.4 years in ERA-Interim (panel (b), see also Dee *et al.* (2011)) but longer than that found in Cy35r3 by Orr *et al.* (2010), who ascribed this error to an excessive amount of parametrized momentum flux near the equator and weak tropical upwelling (Dunkerton, 1997). In addition, the easterly phase of the QBO is too weak in ERA-20CM where at 50 hPa the easterlies peak at about $10-15\,\mathrm{m\,s^{-1}}$ whereas in ERA-Interim they reach about $20\,\mathrm{m\,s^{-1}}$. This error can be improved by reducing the vertical diffusion in the model (Tim Stockdale and Peter Bechtold, personal communication). The phase of the QBO is different in each member of the ensemble (not shown). The easterly phase of the SAO appears to be reasonably well simulated in boreal wintertime, but in summertime wind speeds in excess of $30\,\mathrm{m\,s^{-1}}$ are at least 50% greater than in ERA-Interim

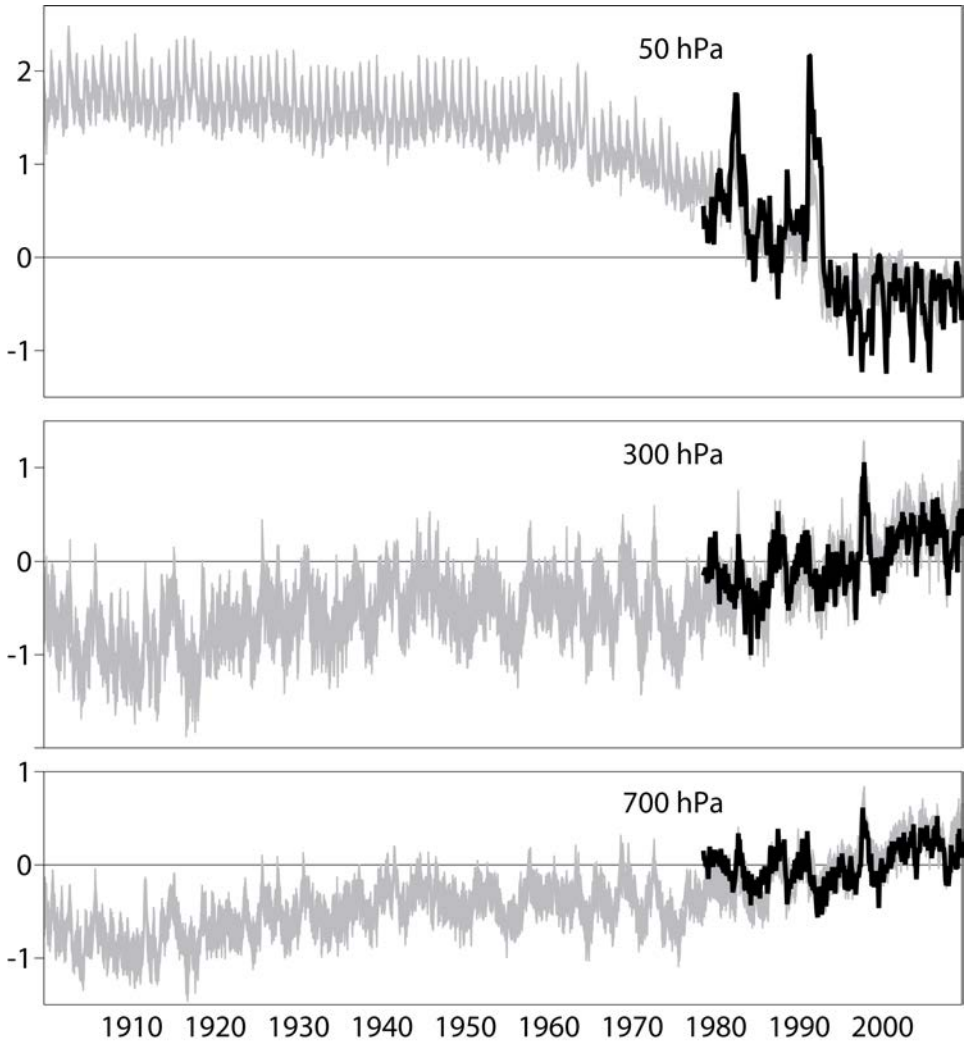

Figure 15: Anomalies relative to 1980-2009 in monthly and globally averaged temperatures (K) at 50, 300 and 700hPa for ERA-20CM ensemble members (grey) and ERA-Interim (black).

(Figures 13, 14). The descending westerly phase of the SAO is not captured in ERA-20CM.

Panels (b), (d) and (f) of Figure 12 show the difference of the 2000-2009 average (colours) with respect to the model climate averaged over the entire 20th century (contours). Features of note are a warming maximum in the tropical upper troposphere and widespread stratospheric cooling that increases with height. An enhanced near-surface warming is apparent over the Arctic, most likely the result of receding sea ice. The upper parts of the jets have slightly intensified and the upper troposphere has become wetter.

Detailed variations over time in global-mean tropospheric and stratospheric temperatures from ERA-20CM have been reported separately by Simmons *et al.* (2013), who compared changes over the final three decades with corresponding changes from the ERA-Interim and MERRA (Rienecker *et al.*, 2011) reanalyses.

A more detailed view of the temporal evolution of temperature at 50, 300 and 700hPa is shown in Figure 15. It displays anomalies relative to 1980-2009, and a comparison with ERA-Interim as well. ERA-20CM exhibits less short-term warming of the lower and middle stratosphere following the eruptions of

El Chichón and Pinatubo than ERA-Interim, which itself provides a slight underestimate. ERA-Interim shows some relatively cold months between 1996 and 2006 that are not seen in ERA-20CM, but the model runs and reanalysis are in general agreement as to the extent of the lower stratospheric cooling since 1979, and when within the period it occurs. There is also generally good agreement between ERA-20CM and ERA-Interim at 300 and 700hPa, both as regards inter-annual variability and the differences in warming rate between the two levels. Overall warming since 1979 is a little lower in ERA-Interim than ERA-20CM, particularly in the lower troposphere, but there are reasons discussed by Simmons *et al.* (2013) to suppose that warming is underestimated in ERA-Interim. Changes in global-mean temperature throughout the troposphere in ERA-20CM are broadly similar to those for SST shown in Figure 2, and to near-surface temperature over land that will be discussed in Section 7.1, in that they rise to a maximum in the 1940s after a decline in the first few years, decline slightly until the mid 1970s, and then rise again until the early 2000s.

Although differences of detail higher in the stratosphere are noted by Simmons *et al.* (2013), the strong cooling seen in ERA-20CM was reproduced in general by both ERA-Interim and MERRA. Both reanalyses were constrained in the upper stratosphere by the assimilation of data from the Stratospheric Sounding Unit (SSU; 1979-2006) and Advanced Microwave Sounding Unit (AMSU; 1998 - present).

7 Long-term variation in two-metre temperature

7.1 Annual means

Previous studies such as those performed by Simmons *et al.* (2004), Compo and Sardeshmukh (2009) and Compo *et al.* (2013) have shown that large-scale, low-frequency variations in near-surface air temperature over land can be captured with reasonable fidelity by atmospheric model integrations in which the SST is specified using analysed values. Such integrations cannot be expected to reproduce actual synoptic and longer term variability associated with internal atmospheric dynamics and interactions between the atmosphere and the land-surface. They should, however, capture much of the variability on inter-annual and longer time scales, and through the use of ensembles should sample the remaining internal variability, as well as, in the case of ERA-20CM, the variability associated with uncertainty in knowledge of the sea-surface temperature.

This is illustrated by comparison with the CRUTEM4 analyses of monthly station climatological temperatures for 5^o grid boxes (Jones et al., 2012). Computational details are as in Simmons *et al.* (2010). The top panel of Figure 16 shows annual-mean anomalies relative to 1961-1990 for area-weighted averages over all grid boxes where CRUTEM4 provides values, for CRUTEM4 itself and the ERA-20CM ensemble mean. El Niño events are marked by ticks on the time axis that denote months for which the SST anomaly averaged over the Niño 3.4 region (120-170W; 5N-5S) was greater than 1K; the height of each tick is proportional to the extent to which the 1K threshold was exceeded. In this case the anomaly is calculated relative to a 361-month mean centred on the month in question where possible, though necessarily fixed at the beginning and end of the period. The two calendar years following the volcanic eruptions of Santa Maria, Agung, El Chichón and Pinatubo are also marked.

The ERA-20CM ensemble mean evidently reproduces the long-term variations in temperature over land identified in CRUTEM4, with warming over the first and last few decades of the 20th Century and a smaller net cooling from around 1940 until the mid 1970s. ERA-20CM's bias relative to CRUTEM4 changes sign from one of these periods to another, as discussed below when considering decadal means. ERA-20CM also reproduces shorter-term variability, with a tendency for relatively cool years following

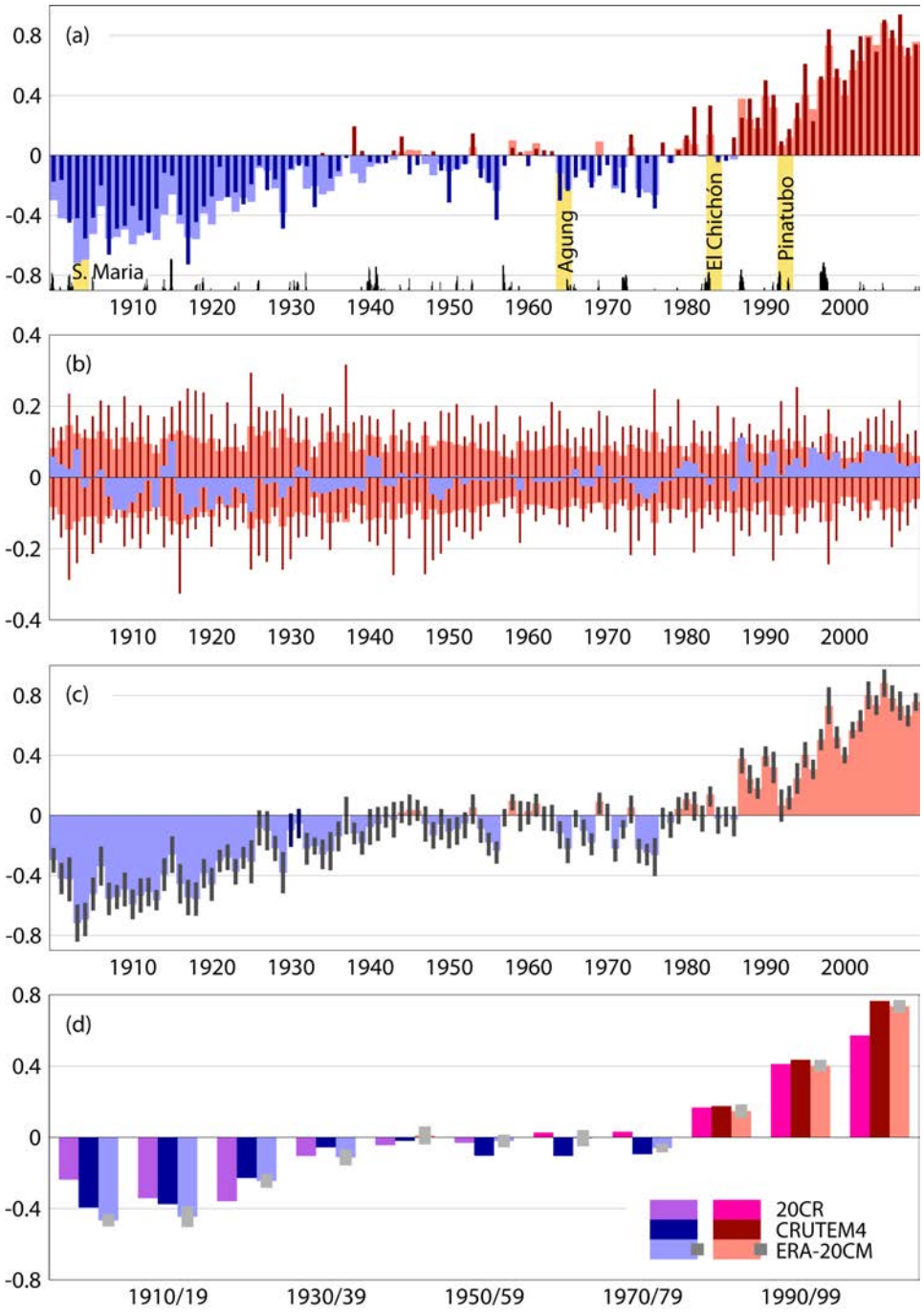

Figure 16: (a) Annual-mean temperature anomalies (K) relative to 1961-1990 for the ERA-20CM ensemble mean (broader, lighter-coloured bars) and CRUTEM4 (version 2.0.0 from www.metoffice.gov.uk/hadobs; narrower, darker-coloured bars) for area-weighted averages taken over all grid boxes for which CRUTEM4 has values. Timings of El Niño events and volcanic eruptions are indicated as described in the text. (b) The range of the annual-means of the ERA-20CM ensemble members (darker, narrower bars), their ± one standard deviation range (broader, pink bars), and the difference between the all-land average and the average sampled as CRUTEM4 for the ensemble mean (blue bars). (c) As (a) for the ERA-20CM ensemble mean, but showing also the ± one standard deviation range (grey bars) of the annual-mean anomalies for individual ERA-20CM ensemble members. (d) Decadal-mean anomalies relative to 1900-2009 for ERA-20CM and CRUTEM4, and the ± one standard deviation range of the decadal-mean anomalies for individual ERA-20CM ensemble members (centre and right bars, colours as in other panels); also shown are the decadal mean anomalies from the NOAA-CIRES 20th Century Reanalysis Version II (left bars).

the major volcanic eruptions and warm years following El Niño SST maxima. Interpretation is complicated, however, by joint occurrences of the two types of event. The change from 1991 to 1992 is a case in point: the mean of a set of CMIP5 simulations (which on average would not be expected to reproduce the observed El Niño) indicates a fall in global-mean surface temperature of around 0.35K due to stratospheric aerosol from the eruption of Pinatubo (Forster *et al.*, 2013), whereas ERA-20CM has warm El Niño tropical Pacific temperatures and produces a net drop in global-mean temperature close to the observed value of around 0.2K. In other cases, such as 1983, discrepancies between modelled and observed values that could have their origin in either intrinsic variability or model error come into play.

The inter-ensemble variability of annual means is illustrated in the middle panels of Figure 16. Panel (b) shows the temperature range that lies within one standard deviation of the ensemble mean and the range from warmest to coldest member relative to the ensemble mean. Panel (c) superimposes the $\pm$ one standard deviation range on the ensemble-mean anomalies. Although inter-ensemble variability decreases somewhat over the first part of the period, it changes little over the second half despite a reducing uncertainty of the prescribed SSTs, and is generally much larger than the spread in the 365-day means of the SSTs shown in panel (b) of Figure 1. The inter-ensemble spread thus appears, on longer timescales at least, to arise mostly from the internal variability of the modelled system triggered by the differences in SST however large or small, rather than from a response forced directly by the SST variations. From panel (c) it can be seen that many changes from one year to the next in the ensemble mean are within the one standard deviation range. Several but not all of the quite small number of cases where change lies outside this range are associated with the identified El Niño and volcanic events.

Panel (b) also shows (blue bars) the differences between all-land averages for the ERA-20CM ensemble mean and corresponding averages made with the same spacial sampling as CRUTEM4, which is what is plotted otherwise in Figure 16. These differences are generally small, improving confidence in the long-term trends shown in panel (a), as the CRUTEM4 data coverage varies quite substantially over time. The differences do show a trend, however, from values that are mainly negative in the first half of the period to values that are quite consistently positive towards the end of the period. This is to be expected due to under-sampling by CRUTEM4 of high northern latitudes where warming is strongest, as discussed for example by Simmons *et al.* (2010) for earlier CRUTEM versions and by Jones *et al.* (2012) for CRUTEM4 itself. In addition, grid boxes over the USA contribute more to the average over all grid boxes in the early years than they do later on, when data coverage is more uniform, ERA-20CM is biased cold relative to CRUTEM4 over the USA in the early years, as illustrated and discussed later.

7.2 Decadal means

The bottom panel of Figure 16 shows decadal averages. Results are shown not only for ERA-20CM and CRUTEM4, but also for Version II of the NOAA-CIRES 20th Century Reanalysis (20CR; Compo *et al.* (2011)). The $\pm$ one standard deviation range for the ERA-20CM decadal means is also shown. In this case anomalies are shown relative to the full 1900-2009 period, as this provides the best basis for examining shifts in bias over time.

The ERA-20CM ensemble mean is close to but slightly below CRUTEM4 for the last three decades. It is biased more substantially cold relative to CRUTEM4 for the first four decades, and biased warm for the intermediate decades; over many of these decades the difference between the ensemble mean and CRUTEM4 is distinctly larger than the standard deviation among ensemble members. 20CR is quite similar to ERA-20CM and CRUTEM4 for several of the decades, but differs from the ERA-20CM ensemble mean by more than 0.1 K for the first three decades and the last one, and in three of the four cases it is further from CRUTEM4 than ERA-20CM. The standard deviation of the difference from

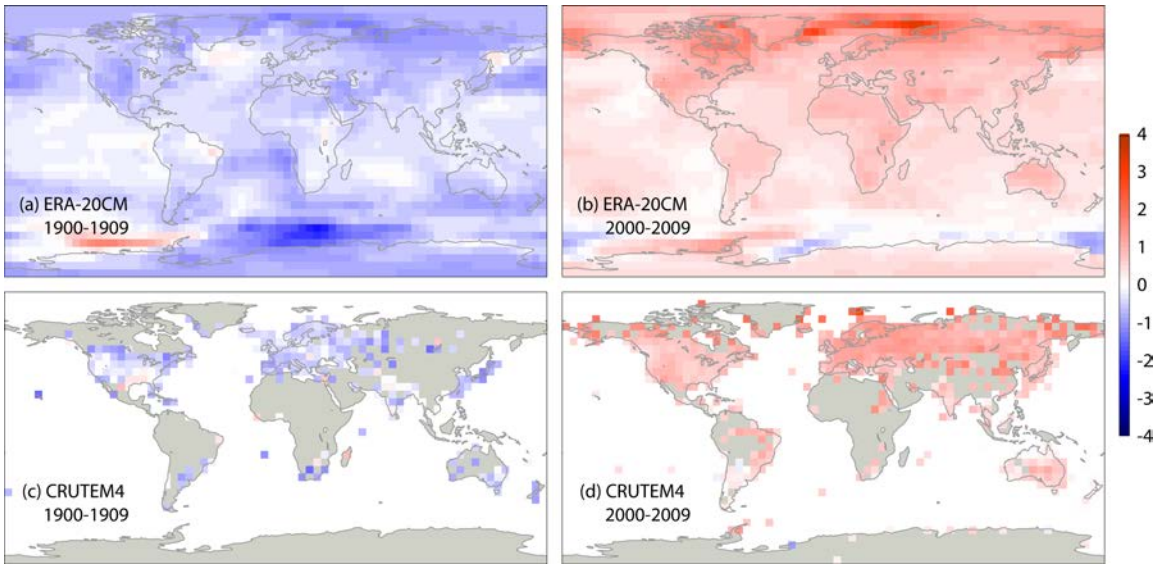

Figure 17: Temperature anomalies (K) relative to 1961-1990. Mean maps for the decades 1900-1909 (a, c) and 2000-2009 (b, d) are shown for the ERA-20CM ensemble mean (a, b) and CRUTEM4 (c, d). ERA-20CM values are averaged over the 5O CRUTEM4 grid boxes. CRUTEM4 values are plotted only for grid boxes with complete monthly coverage for the decade in question.

CRUTEM4 decadal means is 0.11K for 20CR and 0.06K for the ERA-20CM ensemble mean. For annual means the standard deviations of the differences from CRUTEM4 are 0.14K for 20CR and 0.12K for the ERA-20CM ensemble mean.

Compo *et al.* (2013) note that 20CR exhibits better agreement with CRUTEM4 than its own model equivalent to ERA-20CM, termed AMIP20C. The implied beneficial effect on temperature of constraining the synoptic situation by assimilating surface-pressure observations in 20CR may also explain why 20CR is more competitive with ERA-20CM on the annual than on the decadal time scale. Consistent with this, the standard deviations for monthly means are smaller for 20CR: 0.21K compared with 0.29K. Nevertheless, the fact that ERA-20CM outperforms 20CR on the annual scale and longer is a reminder that key components of a good long-term atmospheric reanalysis are the quality of the assimilating atmospheric model and the quality of the prescribed analyses of SST and sea-ice distributions.

Figure 17 compares maps of the mean temperature anomalies for 1900-1909 and 2000-2009 relative to 1961-1990. Overall warming over time is evident. Warming in recent decades occurs over virtually all land areas in ERA-20CM and where sampled in CRUTEM4; in contrast there are a few land areas where 1900-1909 is hardly colder or even slightly warmer than 1961-1990. Recent warming is generally larger over land than sea, but is especially large where sea-ice cover has declined at high northern latitudes. A more mixed picture is seen around Antarctica.

A particularly interesting feature of Figure 17 is that one of the regions where 1900-1909 is warmer than 1961-1990 in CRUTEM4 is the southern USA, and other parts of the USA are hardly colder in the earlier decade. This is not the case for the ERA-20CM ensemble mean, as can be seen in Figure 17, nor is it the case for any ensemble member. This behaviour is seen for other decades prior to the 1940s, and 1950-1959 is generally warmer relative to 1961-1990 in CRUTEM4 than ERA-20CM for much of the USA. It is a significant contributing factor to the cold bias of ERA-20CM relative to CRUTEM4 seen for the first four decades in Figure 16.

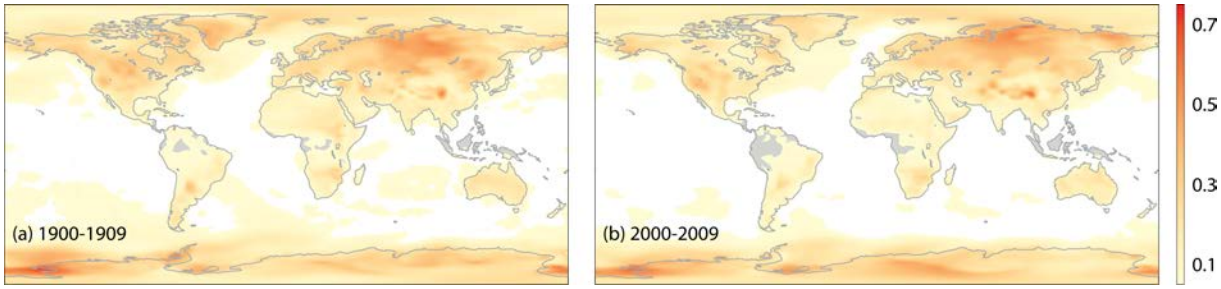

Figure 18: Standard deviations of decadal-mean temperatures for (a) 1900-1909 and (b 2000-2009 (K) among members of the ERA-20CM ensemble.

Compo *et al.* (2013)'s supplementary Figure S2 is relevant in this regard. It shows the linear trends in 2m temperature over 1901-2010 for 20CR, AMIP20C, CRUTEM4 and five other datasets based on analysis of station records of near-surface air temperature. There is some variation among the alternative analyses of the station data, but all show slight cooling at some locations in the southern USA, and little warming in general over the eastern part of the country. 20CR shows quite strong cooling over most of the USA, one of a few regions that contribute to the net underestimation of trend indicated by the decadal-mean plots in Figure 16. The corresponding model run, AMIP20C, shows warming over the USA, and is similar to ERA-20CM in this respect.

The cooling bias over the USA in 20CR suggests a specific problem in the assimilation of surface-pressure observations, but the reason why both ERA-20CM and AMIP20C show a warm bias relative to the analysed station data is at present unclear. Investigation is beyond the scope of this paper, but needed for the improvement it might bring to future products.

The inter-ensemble standard deviations of decadal means are shown in map form in Figure 18, again for 1900-1909 and 2000-2009. Low values over sea, especially for the recent decade, are indicative of the control exerted by the SST on the near-surface marine air temperatures. That the spread of the ensemble is so much larger over land than sea, and is generally similar in pattern for the two decades, is further evidence that it is associated with internal variability rather than a directly forced response to variability in SST. Variability is highest over Siberia, the north-eastern part of the Tibetan Plateau and around the coast of Antarctica in the two decades shown in Figure 18. This is the case more generally, although variability over North America is comparable with that over Siberia in several other decades.

7.3 Changes in global-mean temperature over recent decades

Enough residual internal variability finds its way into five- and ten-year means of globally averaged temperature (including sea as well as land areas) for there to be quite substantial variability among ERA-20CM ensemble members in the rate of warming over spells within the past forty years, even if all members produce a largely similar net change over the whole period. This is relevant to discussion of the recent slowdown in global warming, following a period of rapid temperature rise in the 1980s and 1990s. A hiatus is known from coupled atmosphere-ocean climate modelling to be possible, due to internal variability of the climate system (see http://www.metoffice.gov.uk/research/news/recent-pause-in-warming, and references therein) and it is of interest to see from ERA-20CM how much variability in the rate of warming can occur even with constrained SSTs.

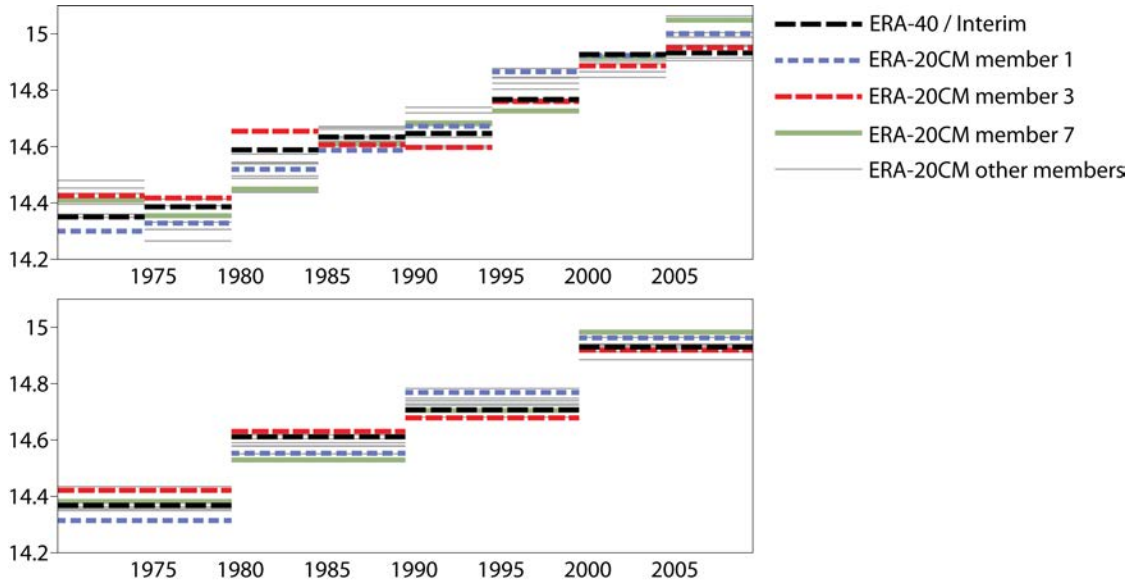

Figure 19: Five-year (upper) and ten-year (lower) averages of global-mean 2m temperature (K) for 1970-2009, from a mix of ERA-40 and ERA-Interim and from ERA-20CM ensemble members, three of which are highlighted. ERA-40 data are used from 1970 to 1978 and ERA-Interim from 1979-2009. The ERA-40 values are adjusted by the mean difference between ERA-Interim and ERA-40 over their common 1979-2001 period, and the resulting amalgamated values are adjusted to have the same 1970-2009 mean value as the ERA-20CM ensemble mean.

Figure 19 shows five- and ten-year averages of global-mean two-metre temperature spanning 1970-2009, for the ERA-20CM ensemble members and for a combination of the ERA-40 and ERA-Interim reanalyses. Three ensemble members are highlighted because of their different behaviour. Member 3, shown in red, is noteworthy because after a large jump in the five-year mean values between 1975-1979 and 1980-1984, its five-year means decline over the next two periods; it is the warmest member for 1980-1984 but the coldest for 1990-1994. Its decadal means show very little warming between 1980-1989 and 1990-1999. In contrast, member 7 (green solid) shows strong warming in the five-year means between 1980 and 1995, and member 1 (blue dashed) shows substantial decadal-mean warming between 1980-1989 and 1990-1999. In the light of the variability exhibited by ensemble members, the almost complete absence of warming in ERA-Interim between 2000-2004 and 2005-2009 averages does not look remarkable. These findings are in line with Kosaka and Xie (2013), who present evidence that the current inferred hiatus is part of internal climate variability tied to La-Niña cooling, but the results presented here show that internal variability may also cause marked differences in atmospheric warming in periods characterized by warming SSTs.

8 Aspects of the hydrological cycle

8.1 Near-surface humidity over land

Simmons *et al.* (2010) reported a reduction in relative humidity over low- and mid-latitude land areas over ten years up to 2008, based on both ERA-Interim and an extension of the HadCRUH analysis of station data (Willett *et al.*, 2008). Relative humidity has since remained lower than in the last decades of the 20th century (Willett *et al.*, 2013). This was interpreted by Simmons *et al.* (2010) to be a consequence

of limited moisture supply from the oceans, whose surface temperatures have not risen in concert with near-surface air temperatures over land in recent years. ERA-20CM helps place these results in context.

The upper panel of Figure 20 shows twelve-month running means of two-metre temperature averaged separately for land and sea for each of the ERA-20CM ensemble members, and also for the ERA-20CM ensemble mean and ERA-Interim over land. It illustrates how unusual recent years have been in that it is only for these years that the anomalies in temperature over land of all ensemble members exceed the anomalies in temperature over sea, which at two-metre height are strongly constrained by the prescribed SSTs. It also illustrates the much greater inter-ensemble temperature variability over land than over sea noted previously. The good agreement between ERA-20CM and ERA-Interim as regards temperature variations over land is to be expected given the known good agreement between ERA-Interim and CRUTEM4, and the agreement between ERA-20CM and CRUTEM4 discussed above.

The middle panel of Figure 20 shows corresponding plots for dew-point depression at two-metre height. Dew-point depression is the near-surface atmospheric humidity variable that can be extracted from the monthly-mean data archived from ERA-20CM, and is related more closely to relative humidity (Lawrence, 2005) than specific humidity. The bottom panel shows results for the model's top-layer soil moisture, which has a depth of 7cm. Both panels show that the final decade of ERA-20CM is exceptional in terms of the duration and maximum extent of dry values over land, where dryness here means in effect relative rather than specific humidity for the atmosphere, but water content for the soil. The behaviour of ERA-Interim appears to be more extreme than the average behaviour of ERA-20CM, though, as is seen from the top-right corner of panel (b), one of the ten ensemble members becomes drier than ERA-Interim close to the end of the period. Dew-point depression is largely uniform over sea in these averages, but does show a slight decline over recent years, indicating a slight recent increase in the relative humidity of the near-surface marine atmosphere in the ERA-20CM simulations.

8.2 Total column water vapour over oceans

The net amount of moisture in the atmosphere increases over time in ERA-20CM, as expected with increasing temperature. The increase in total column water vapour shows very similar behaviour over land and sea, even for recent years. This is shown in the top panel of Figure 21. The other two panels of the figure provide further information relating to the values over sea, for which there is direct observational data only for the last three decades, and which have proved generally problematic for reanalysis. Twelve-month running means are displayed. The middle panel of Figure 21 shows total column water vapour over ice-free sea for ERA-20CM, for both actual modelled values and proxy values based on a known correlation between total column water vapour and SST (Trenberth *et al.* (2005), Uppala *et al.* (2005)). Specifically, the proxy is proportional to the saturation specific humidity computed using the monthly ensemble-mean SST and surface pressure, with the constant of proportionality determined subjectively to give about the same range of variability as the actual model values. Also shown for the end of the period are version-6 SSMI retrievals from Remote Sensing Systems (Wentz, 1997), adjusted to have the same average as the ERA-20CM ensemble mean over the period (July 1987 to September 2009) for which reliable retrievals are available. The panel shows good agreement between model and proxy values throughout, and the variations in both match well the variations in SSMI retrievals. These results provide support for the view that low frequency variability and trends in total column water vapour over the ocean are strongly controlled by SST, and that values over land are constrained by moisture supply from the oceans to vary similarly, as shown previously for near-surface specific humidity from HadCRUH and ERA-Interim (Simmons *et al.*, 2010).

Absolute values of total column water vapour from ERA-20CM, retrievals and ERA-Interim are shown in

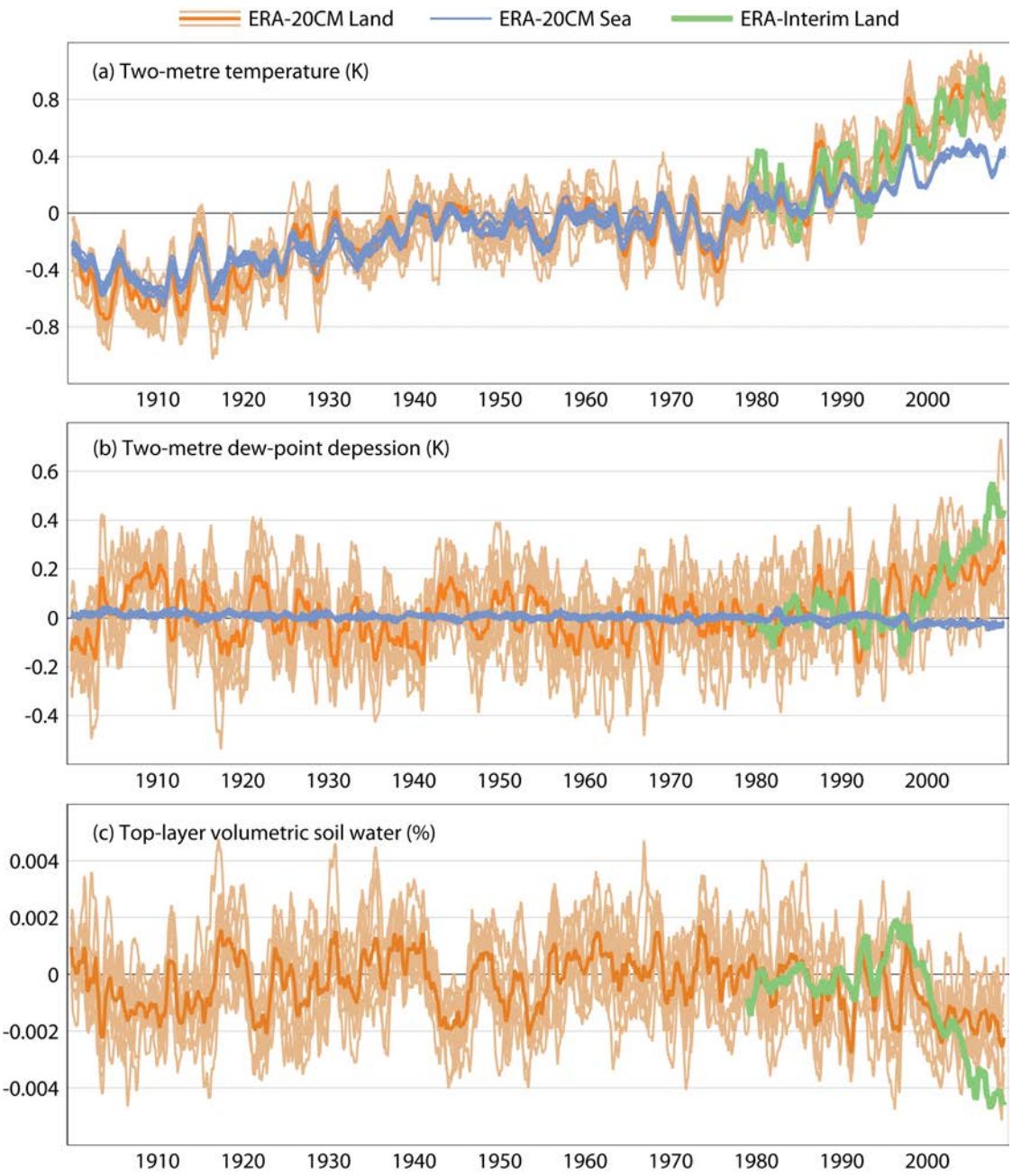

Figure 20: Twelve-month running mean anomalies relative to 1961-1990 for: (a) two-metre temperature (K); (b) two-metre dew-point depression (K); (c) the model top-layer volumetric soil water (%). Results are shown over land for the ERA-20CM ensemble members and ensemble mean (orange), and for ERA-Interim values (green; adjusted to have the same average as the ERA-20CM ensemble mean for 1979-2009). Values of two-metre temperature and dew-point depression are also shown over sea for the ERA-20CM ensemble members (blue).

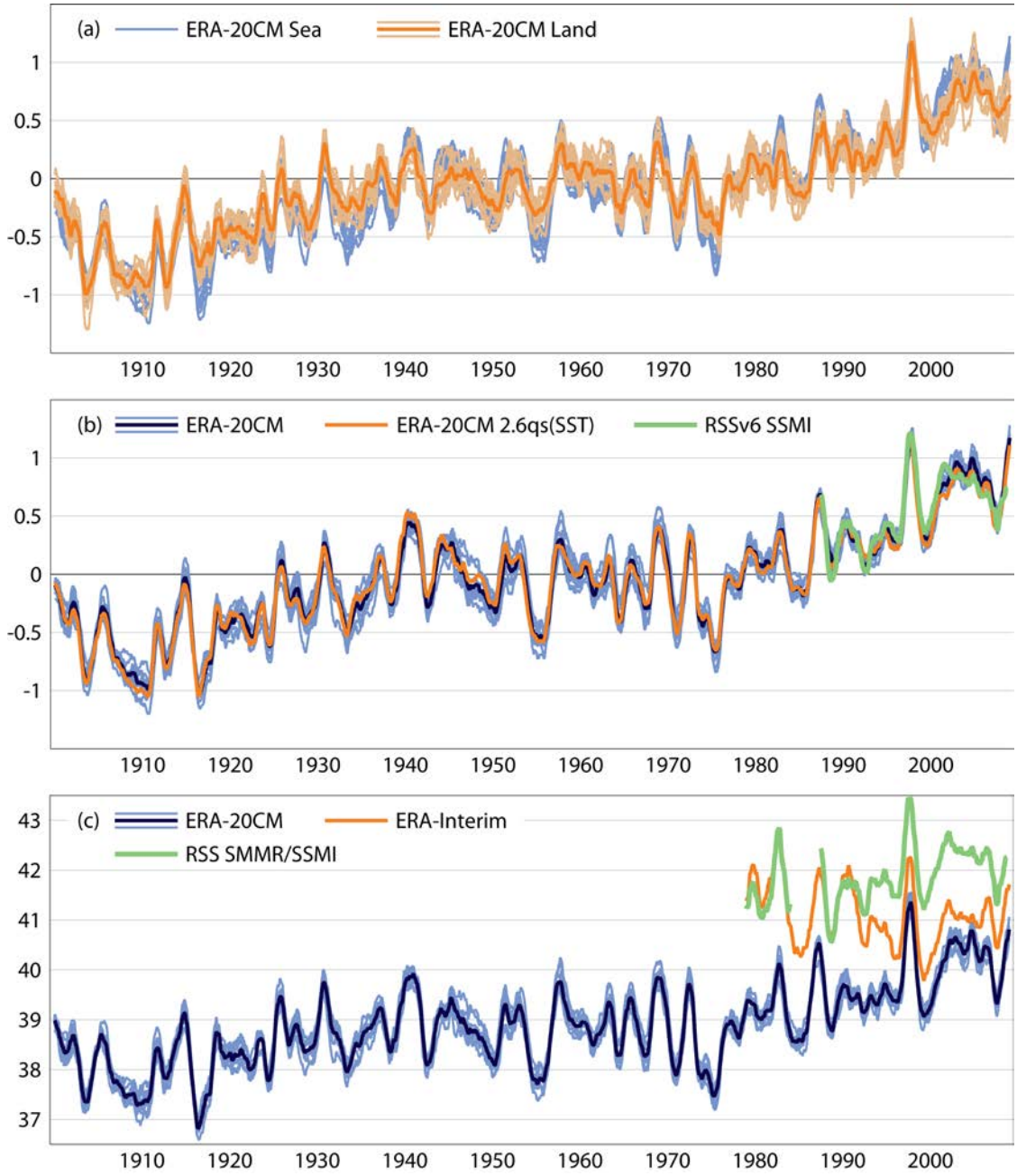

Figure 21: Twelve-month running-mean values of total column water vapour (kgm^{-2}): (a) anomalies relative to 1961-90 for ERA-20CM averages over land (orange) and sea (blue) for each ensemble member and for the ensemble mean over land; (b) anomalies relative to 1961-1990 for averages over ice-free sea from ERA-20CM (blue; ensemble members and ensemble mean), from a proxy derived by multiplying by 2.6 the saturation specific humidity (in g/kg) computed for the ensemble-mean sea-surface temperature and surface pressure (orange), and from version-6 SSMI retrievals from Remote Sensing Systems (green; adjusted to have the same average as the ERA-20CM ensemble mean over the period for which data are available); (c) averages over tropical seas from ERA-20CM (blue; ensemble members and ensemble mean), from ERA-Interim (orange), and from SMMR and version-6 SSMI retrievals from Remote Sensing Systems (green).

the bottom panel of Figure 21. In this case the average is taken only over the tropical belt, to enable comparison to be made with retrievals from SMMR data for 1979-1984 (Wentz and Francis, 1992). SMMR data were not assimilated in ERA-Interim; SSMI radiances were. ERA-20CM values are evidently biased dry compared with both SMMR and SSMI retrievals, though temporal variability (related to SST variations as discussed above) is closely matched. In contrast, ERA-Interim values match closely the SMMR retrievals and also the SSMI retrievals until the end of 1991, but thereafter are biased dry. This is because the early version of the scheme for assimilating rain-affected SSMI radiances used in ERA-Interim had a pronounced and erroneous drying effect (Geer *et al.* (2008); Dee *et al.* (2011)). The effect is seen only from the beginning of 1992 as the amounts of data assimilated earlier from the rain-sensitive SSMI channel were very small.

8.3 Hydrological balance

The atmospheric model used for ERA-20CM does not enforce long-term global hydrological balance, but its degree of imbalance is found to be highly stable. Anomalies in global-mean precipitation and evaporation on annual and longer timescales match closely, and the residual small imbalance fluctuates around zero.

This is shown in the upper two panels of Figure 22, which presents twelve-month running means for the ERA-20CM ensemble mean. Panel (a) shows the global means of precipitation and evaporation, and their difference. The absolute values of precipitation and evaporation are similar but not quite the same. They differ by around 0.1 mm/day, about 4% of their values. Small oscillations and a slight upward trend can be discerned for both precipitation and evaporation, but not for their differences in this particular plot.

Detail can be seen in panel (b), which shows anomalies relative to 1961-1990. Evaporation is not shown as it is so similar to precipitation. This can be inferred from the small values of the plotted differences. Both precipitation and evaporation rise from around 1910 to 1940 and from the mid 1970s, and fall in the intervening period, as is the case for temperature. Relatively large values occur in conjunction with the 1997/98 El Niño.

The lower panels, (c) and (d), present the contributions to the global means from sea and land areas. They show that variations are in general larger over sea than land, but that the variations in precipitation over sea tend to be matched by similar variations in evaporation. In particular, both precipitation and evaporation over sea increase from the mid 1970s onwards, but increases in land values are much less clear, especially if the relatively high land values during and immediately after the 1997/98 El Niño can be discounted. This is an interesting result, as Durack and Wijffels (2010) concluded from a study of an extensive set of measurements of ocean salinity that salty, evaporation-dominated regions of the world's oceans were becoming saltier, and relative fresh, precipitation-dominated regions were becoming fresher, and noted that the implied changes in oceanic precipitation and evaporation were consistent with an amplification of the global hydrological cycle. The ERA-20CM model results indicate that increases in precipitation and evaporation over the oceans do not necessarily imply corresponding increases in precipitation (and evaporation or run-off) over land.

The behaviour shown for the ensemble mean in Figure 22 is found also for individual ensemble members. Figure 23 presents the contributions to the global means of precipitation and evaporation from sea and land for all ensemble members as well as the ensemble mean. Only the period from 1970 onwards is shown to enable detail to be seen better. Some spread around the ensemble mean values can be seen, but the large-amplitude variations are common to all members. Figure 23 also shows precipitation anomalies over land from ERA-Interim. The latter are necessarily with respect to a more recent reference period,

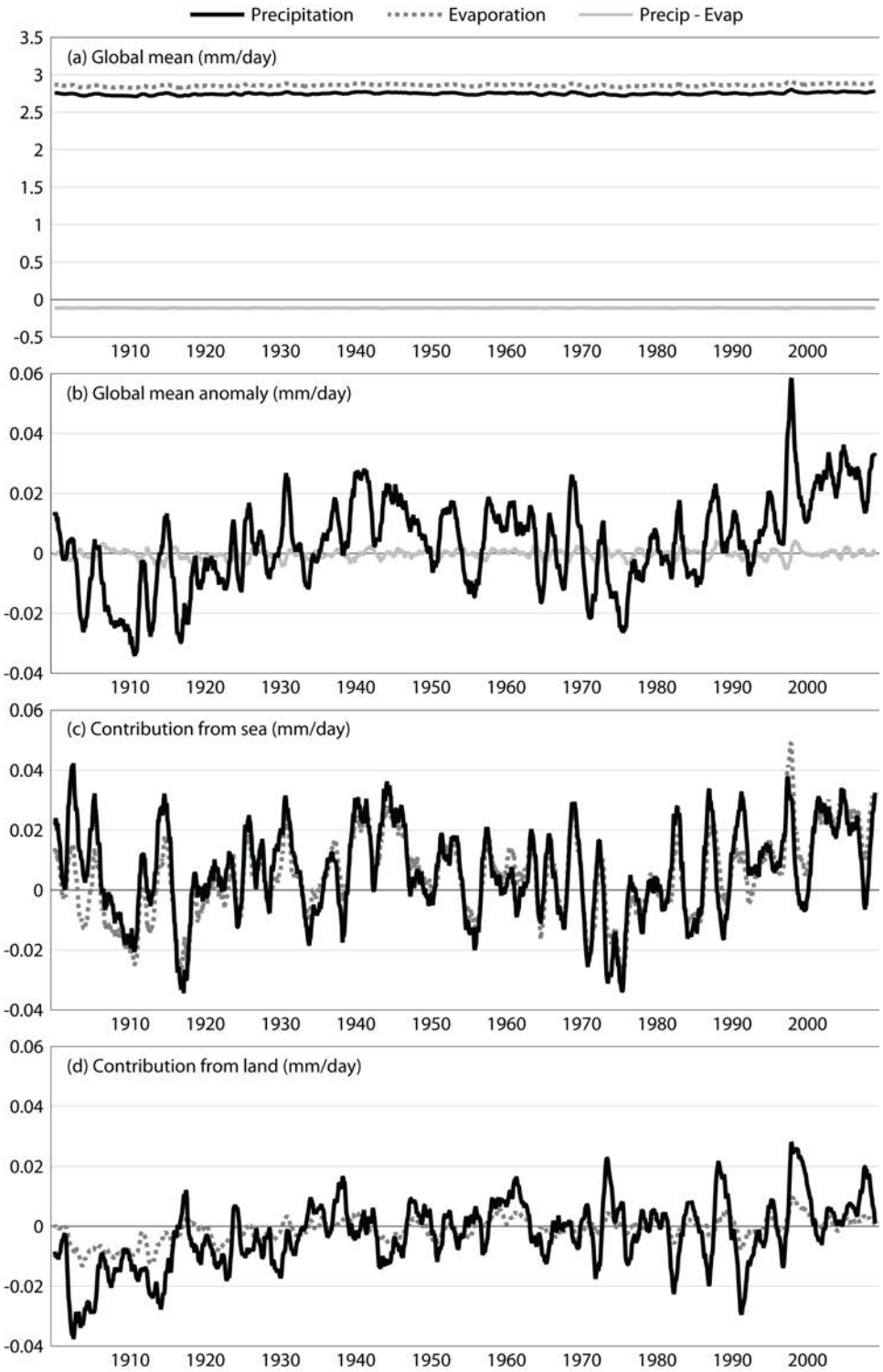

Figure 22: Twelve-month running-mean values of components of the global hydrological budget (mm/day) of the ERA-20CM ensemble mean: (a) Global-mean precipitation (black solid), evaporation (black dotted) and their difference (grey); (b) as (a) but for anomalies relative to 1961-1990, showing precipitation and the difference between it and evaporation; (c) the contribution to the global-mean anomaly from sea areas for precipitation and evaporation; (d) as (c), but for land areas.

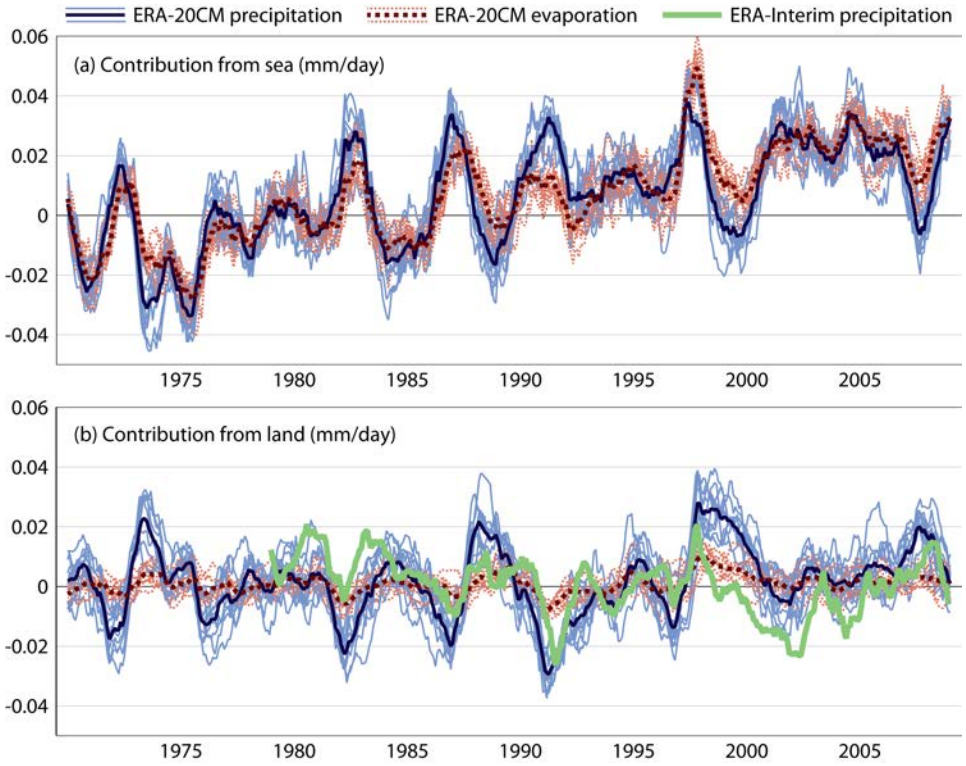

Figure 23: Twelve-month running-mean values of components of the global hydrological budget (mm/day) of the ERA-20CM ensemble mean and members for 1970-2009: (a) the contribution to the global-mean anomaly relative to 1961-1990 from sea areas for precipitation and evaporation; (b) as (a), but for land areas. The anomaly relative to 1981-2010 in ERA-Interim precipitation over land is also shown.

but this makes little difference, as land values show little long-term trend. Comparison with the ERA-20CM values is made poorer by an erroneous long-term variation over time in ERA-Interim rainfall over land, a response to more severe problems over sea discussed by Simmons *et al.* (2013). The variation over sea is beyond the scale of Figure 22, and is not displayed as comparison with ERA-20CM would not be meaningful.

The largest anomalies over land in recent years are the above-mentioned one during and immediately after the 1997/98 El Niño, when ERA-20CM has relatively large excesses of evaporation over precipitation over sea and of precipitation over evaporation over land, and a shorter-lived but slightly larger one peaking in 1991, during which the excess of precipitation over evaporation over land is unusually low, at about 15% of its normal value of around 0.2 mm/day expressed in terms of the contribution to the global-mean budget. A similar minimum in precipitation is seen in ERA-Interim, which also matches other minima and maxima, notwithstanding its erroneous trend from the 1990s to the 2000s. In turn, good agreement between inter-annual variations from ERA-Interim and from the Global Precipitation Climatology Centre (GPCC; Becker *et al.* (2013)) is seen in time series of values averaged over a subset of 1^o land grid squares for which GPCC had access to data from at least one station for every month from 1979 to 2012 (Simmons *et al.*, 2013).

Maps of the spatial distribution of annual- and decadal-mean precipitation from ERA-20CM have been compared with both ERA-Interim and GPCC. Although some robust and expected agreement is found for anomalies in the tropics and subtropics and in a trend for increasing precipitation at high northern latitudes, detailed comparison is not straightforward in view of the presence of both inter-ensemble spread of the temporal means and, doubtless, regionally varying model error. It is beyond the scope of this paper to investigate this further.

9 Conclusion and outlook

Model simulations of the past using prescribed, observationally-based forcings and boundary conditions provide an important tool for understanding and estimating climate change. The ERA-20CM ensemble of model integrations provides a reference climate against which the ERA-CLIM reanalyses can be gauged. Since no atmospheric observations have been assimilated, ERA-20CM is not able to represent the correct synoptic evolution of the atmosphere. All observational information is incorporated in the model boundary conditions and forcing. These account for the evolution of SST, sea ice, solar forcing, ozone, aerosols and greenhouse gases, which include major events such as volcanic eruptions and the El Niño Southern Oscillations. Therefore, as demonstrated in this paper, ERA-20CM provides a good reference for the low-frequency variability of the atmosphere for the 20th century, and is well suited to project global warming and major events onto other geophysical quantities that are not directly provided in the forcing data.

Two-metre temperature follows trends in the prescribed HadISST2 forcing, with an amplified climate signal over land in recent years. The ERA-20CM ensemble evidently reproduces the long-term variations in temperature over land as identified in CRUTEM4. ERA-20CM also reproduces shorter-term variability, with a tendency for relatively cool years following the major volcanic eruptions and warm years following El Niño SST maxima. The ERA-20CM ensemble mean is close to but slightly below CRUTEM4 for the last three decades. Up to the yearly timescale ERA-20CM is found to outperform the NOAA/CIRES 20CR reanalyse, while on shorter time scales, where the correct synoptic situation is essential, the picture is reversed. Ensemble spread over land is mainly driven by internal model variability, while over sea, variation in temperature is more closely related to the spread in the HadISST2 ensemble.

Low frequency variability of total column water vapour also follows trends in SST (directly over the ocean and indirectly over land). The increase of evaporation over the last decades predominantly rains out over the ocean, leading to a decrease in relative humidity over land.

Although no synoptic atmospheric observations have been assimilated, this lack avoids the risk of adding false climate signals due to an evolving observing system. For this reason, it is less difficult to achieve 'climate quality' trends for ERA-20CM than it is for a long-term atmospheric reanalysis.

Model behaviour is found to be particularly good in the lower troposphere. However, ERA-20CM does exhibit some clear biases. Compared to ERA-Interim, ERA-20CM is biased cold and dry in the higher troposphere and around the tropopause, while it is biased warm in the upper part of the stratosphere. The QBO is represented, however due to the lack of observations and sub-optimal parametrisation, its phase and period are incorrect. The westerly phase of the SAO is far too weak. The net energy flux at the TOA and surface are incorrect by about 1.5 $\mathrm{Wm}^{-2}$and 1 Wm^{-2}, respectively, and have the wrong sign. Although the magnitude of these net fluxes is small compared to the TOA incident solar radiation (~ 340 Wm^{-2}) and smaller than e.g. found for ERA-Interim, it is not small compared to the net energy flux of around 0.9 Wm^{-2}into the ocean in recent decades, as estimated by Trenberth *et al.* (2009). In addition the total energy input and the difference between net precipitation and evaporation is non-zero. For a century-long model integration these quantities should be much closer to zero, but apparently their small but systematic diagnostic imbalance is counterbalanced by terms that are not accounted for, for example due to the dry mass fixing.

Despite these model biases, the trends in ERA-20CM are generally found to be realistic. Regarding energy budgets, e.g., the net outward TOA energy flux of about 1.5 Wm^{-2} between 1940-1970, when no climate drift was observed, does shrink by about 1 Wm^{-2} from 1980, which corresponds well with the estimated trend. Important ingredients of ERA-20CM are the enforced SST and sea-ice cover. For this reason an incorrect net flux cannot influence the ocean surface, and vice versa the enforced HadISST2 dictates the maritime two-metre temperature, regardless of the model energy budgets. In this respect, ERA-20CM has less difficulties in approaching 'climate quality' at lower levels than an ocean-atmosphere coupled system would have in a similar environment of model bias.

It is desirable to minimize model bias, and to ensure that the net energy flux cancels out for the middle part of the 20$^{\mathrm{th}}$ century. This is beyond the scope of this paper. Although the adverse effect on trends is found to be limited for ERA-20CM, model bias is a concern for reanalysis. The evolution of the observing system will slowly draw the model analysis away from the model climate when data is sparse towards the climate formed by the observing network when coverage is more complete. Variational bias correction schemes are designed to correct observation bias, rather than model bias. It relies on redundancy within the observing system and requires some known unbiased observations (anchors); conditions that are not satisfied in the first part of the 20$^{\mathrm{th}}$ century. Model bias correction in a variational scheme still requires a considerable amount of research. A pragmatic model retuneing is a less difficult option, but this should be performed with great care.

The ERA-20C reanalysis (Poli *et al.*, 2013) will be based on a later version of the IFS (Cy38r1). In addition, it is forced with HadISST2.1.0.0, which is a newer release than used in ERA-20CM. In order to allow for a closer comparison, a second integration of ERA-20CM is planned that incorporates these upgrades. Other points of future attention are the inclusion of the CMIP5 recommended evolution of black carbon aerosols. ERA-20CM only accounts for the evolution of tropospheric sulphate and stratospheric sulphate, the latter being very important to capture the response of energy fluxes on volcanic activity. The mapping from the total load to a three-dimensional mixing ratio follows the description of the operational ECMWF model, which is rather crude. A more sophisticated scheme using observational

profiles is to be explored. It should be able to better describe the vertical distribution of the change in upper-air temperature due to Pinatubo, which is found to be non-optimal in ERA-20CM. Another area of future improvement is the evolution of the land usage and vegetation. In ERA-20CM it is not varied and follows the operational ECMWF model description. This should allow for a more sophisticated response of land temperature and humidity to the evolution in the prescribed SST and may locally modify trends as reported in this paper.

10 Acknowledgments

The work described in this paper is part of the ERA-CLIM project, and is funded by the Seventh Framework Programme of the European Union under grant agreement no. 265229. The HadISST2.0.0.0 dataset was provided by the Met Office Hadley Centre with partial funding from ERA-CLIM. We acknowledge the World Climate Research Programme's Working Group on Coupled Modelling, which is responsible for CMIP5. We are grateful to the EC-Earth consortium for making available the adaptations that were required for the ingestion of CMIP5 ozone and aerosol data, in particular to Simona Ştefănescu and Shuting Yang. We thank Tim Stockdale, Peter Bechtold, Linus Magnusson and Johannes Flemming for their invaluable help and advice that enabled the realization of ERA-20CM.

References

Balsamo, G., Viterbo, P., Beljaars, A., van den Hurk, B., Hirschi, M., Betts, A. K. and Scipal, K. (2008). A revised hydrology for the ecmwf model: Verification from field site to terrestrial water storage and impact in the integrated forecast system. *ECMWF Tech. Memo. No. 563*.

Bechtold, P., Orr, A., Morcrette, J. J., Engelen, R., Flemming, J. and Janiskova, M. (2009). Improvements in the stratosphere and mesosphere of the ifs. *ECMWF Newsletter*, **120**, 22–31.

Becker, A., Finger, P., Meyer-Christoffer, A., Rudolf, B., Schamm, K., Schneider, U. and Ziese, M. (2013). A description of the global land-surface precipitation data products of the global precipitation climatology centre with sample applications including centennial (trend) analysis from 1901present. *Earth Syst. Sci. Data*, **5**, 71–99, doi:10.5194/essd-5-71-2013.

Bengtsson, L., Hagemann, S. and Hodges, K. (2004). Can climate trends be calculated from reanalysis data? *J. Geophys. Res.*, **109**, doi:10.1029/2004JD004536.

Berrisford, P., Dee, D., Poli, P., Brugge, R., Fielding, K., Fuentes, M., Kållberg, P., Kobayashi, S., Uppala, S. and Simmons, A. (2011a). The era-interim archive version 2.0. *Ecmwf era report series*, ECMWF, Shinfield Park, Reading, 13.

Berrisford, P., Kållberg, P., Kobayashi, S., Dee, D., Uppala, S., Simmons, J., Poli, P. and Sato, H. (2011b). Atmospheric conservation properties in era-interim. *Quart. J. Roy. Meteor. Soc.*, **137**, 13811399.

Boussetta, S., Balsamo, G., Beljaars, A., Kral, T. and Jarlan, L. (2011). Impact of a satellite-derived leaf area index monthly climatology in a global numerical weather prediction model. *ECMWF Tech. Memo. 640*.

Cionni, I., Eyring, V., Lamarque, J. F., Randel, W. J., Stevenson, D. S., Wu, F., Bodeker, G. E., Shepherd, T. G., Shindell, D. T. and Waugh, D. W. (2011). Ozone database in support of cmip5 simulations:

results and corresponding radiative forcing. *Atmos. Chem. Phys. Discuss.*, **11**, 10875–10933, doi: 10.5194/acpd-11-10875-2011.

Compo, G. P. and Sardeshmukh, P. D. (2009). Oceanic influences on recent continental warming. *Clim. Dynam.*, **32**, 333–342, doi:10.1007/s00382-008-0448-9.

Compo, G. P., Sardeshmukh, P. D., Whitaker, J. S., Brohan, P., Jones, P. D. and McColl, C. (2013). Independent confirmation of global land warming without the use of station temperatures. *Geophys. Res. Lett.*, **in press**, doi:10.1002/grl.50425.

Compo, G. P., Whitaker, J. S., Sardeshmukh, P. D., Matsui, N., Allan, R. J., Yin, X., Gleason, B. E., Vose, R. S., Rutledge, G., Bessemoulin, P., Brönnimann, S., Brunet, M., Crouthamel, R. I., Grant, A. N., Groisman, P. Y., Jones, P. D., Kruk, M. C., Kruger, A. C., Marshall, G. J., Maugeri, M., Mok, H. Y., ø Nordli, Ross, T. F., Trigo, R. M., Wang, X. L., Woodruff, S. D. and Worley, S. J. (2011). The twentieth century reanalysis project. *Quart. J. Roy. Meteor. Soc.*, **137**, 1–28, doi:10.1002/qj.776.

Dee, D., D., M. B., Balsamo, G., Engelen, R. and Simmons, A. (2012). Toward a consistent reanalysis of the climate system. *Ecmwf research department memorandum*, ECMWF, Shinfield Park, Reading, 687.

Dee, D. P., Uppala, S. M., Simmons, A. J., Berrisford, P., Poli, P., Kobayashi, S., Andrae, U., Balmaseda, M. A., Balsamo, G., Bauer, P., Bechtold, P., Beljaars, A. C. M., van de Berg, L., Bidlot, J., Bormann, N., Delsol, C., Dragani, R., Fuentes, M., Geer, A. J., Haimberger, L., Healy, S. B., Hersbach, H., Hólm, E. V., Isaksen, L., Kållberg, P., Köhler, M., Matricardi, M., McNally, A. P., Monge-Sanz, B. M., Morcrette, J.-J., Park, B.-K., Peubey, C., de Rosnay, P., Tavolato, C., Thépaut, J.-N. and Vitart, F. (2011). The era-interim reanalysis: configuration and performance of the data assimilation system. *Quart. J. Roy. Meteor. Soc.*, **137**, 553–597, doi:10.1002/qj.828.

Dunkerton, T. (1997). The role of gravity waves in the quasi-biennial oscillation. *JGR*, **102**, 26,053–26,076.

Durack, P. J. and Wijffels, S. E. (2010). Fifty-year trends in global ocean salinities and their relationship to broad-scale warming. *J. Climate*, **23**, 4342–4362, doi:10.1175/2010JCLI3377.1.

Forster, P. M., Andrews, T., Good, P., Gregory, J. M., Jackson, L. S. and Zelinka, M. (2013). Evaluating adjusted forcing and model spread for historical and future scenarios in the cmip5 generation of climate models. *J. Geophys. Res.*, **118**, 1139–1150, doi:10.1002/jgrd.50174.

Fröhlich, C. and Lean, J. (2004). Solar radiative output and its variability: Evidence and mechanisms. *Astron. Astrophys. Rev.*, **12**, 273–320, doi:10.1007/s00159-004-0024-1.

Gates, G. W. (1992). Amip: The atmospheric model intercomparison project. *Bull. Amer. Meteor. Soc.*, **73**, 1962–1970.

Geer, A. J., Bauer, P. and Lopez, P. (2008). Lessons learnt from the operational 1d + 4d-var assimilation of rain- and cloud-affected ssm/i observations at ecmwf. *Quart. J. Roy. Meteor. Soc.*, **134**, 1513–1525, doi:10.1002/qj.304.

Hazeleger, W., Wang, X., Severijns, C., Ştefănescu, S., Bintanja, R., Sterl, A., Wyser, K., Semmler, T., Yang, S., van den Hurk, B., van Noije, T., van der Linden, E. and van der Wiel, K. (2012). Ec-earth v2.2: description and validation of a new seamless earth system prediction model. *Clim. Dynam.*, **39**, 2611–2629.

Hess, P., Koepke, P. and Schult, I. (1998). Optical properties of aerosols and clouds: The software package OPAC. *Bull. Amer. Meteor. Soc.*, **79**, 831–844.

Hollingsworth, A., Engelen, R. J., Benedetti, A., Dethof, A., Flemming, J., Kaiser, J. W., Morcrette, J.-J., Simmons, A. J., Textor, C., Boucher, O., Chevallier, F., Rayner, P., Elbern, H., Eskes, H., Granier, C., Peuch, V.-H., Rouil, L. and Schultz, M. G. (2008). Toward a monitoring and forecasting system for atmospheric composition: The gems project. *Bull. Amer. Meteor. Soc.*, **89**, 1147–1164, doi:10.1175/2008BAMS2355.1.

Janssen, P. A. E. M. (1991). Quasi-linear theory of wind wave generation applied to wave forecasting. *J. Phys. Oceanogr.*, **21**, 1631–1642.

Jones, P. D., Lister, D. H., Osborn, J. J., Harpham, C., Salmon, M. and Morice, C. P. (2012). Hemispheric and large-scale land surface air temperature variations: An extensive revision and an update to 2010. *J. Geophys. Res.*, **117**, D05127, doi:10.1029/2011JD017139.

Kennedy, J. J., Rayner, N., Millington, S. and Saunby, M. (2013). The met office hadley centre sea ice and sea-surface temperature data set, version 2, part 1: sea-surface temperature analysis. **In preparation**.

Komen, G. J., Cavaleri, L., Donelan, M., Hasselmann, K., Hasselmann, S. and Janssen, P. A. E. M. (1994). *Dynamics and Modelling of Ocean Waves*. Cambridge University Press: Cambridge, UK.

Kopp, G., Lawrence, G. and Rottman, G. (2005). The toatal irradiance monitor (TIM): science results. *Solar Phys.*, **230**, 129–139.

Kosaka, Y. and Xie, S.-P. (2013). Recent global-warming hiatus tied to equatorial pacific surface cooling. *Nature*, **Advance online publication**, doi:10.1038/nature12534.

Lamarque, J. F., Bond, T. C., Eyring, V., Granier, C., Heil, A., Klimont, Z., Lee, D., Liousse, C., Mieville, A., Owen, B., Schultz, M. G., Shindell, D., Smith, S. J., Stehfest, E., Aardenne, J. V., Cooper, O. R., Kainuma, M., Mahowald, N., McConnell, J. R., Naik, V., Riahi, K. and van Vuuren, D. P. (2010). Historical (1850-2000) gridded anthropogenic and biomass burning emissions of reactive gases and aerosols: methodology and application. *Atmos. Chem. Phys. Discuss.*, **10**, 7017–7039, doi:acp-10-7017-2010.

Lawrence, M. G. (2005). The relationship between relative humidity and the dewpoint temperature in moist air. *Bull. Amer. Meteor. Soc.*, **94**, 225–233, doi:10.1175/BAMS-86-2-225.

Lean, J., Rottman, G., Harder, J. and Kopp, G. (2005). Sorce contributions to new understanding of global change and solar variability. *Solar Phys.*, **230**, 27–53.

Loveland, T. R., Reed, B. C., Brown, J. F., Ohlen, D. O., Zhu, Z., Youing, L. and Merchant, J. W. (2000). Development of a global land cover characteristics database and IGB6 DISCover from the 1km AVHRR data. *Int. J. Remote Sensing*, **21**, 1303–1330.

Magnusson, L., Alonso-Balmaseda, M., Corti, S., Molteni, F. and Stockdale, T. (2012). Evaluation of forecast strategies for seasonal and decadal forecasts in presence of systematic model errors. *ECMWF Tech. Memo. No. 676*.

Meinshausen, M., Smith, S. J., Calvin, K. V., Daniel, J. S., Kainuma, M. L. T., Lamarque, J.-F., Matsumoto, K., Montzka, S. A., Raper, S. C. B., Riahi, K., Thomson, A. M., Velders, G. J. M. and van Vuuren, D. (2011). The rcp greenhouse gas concentrations and their extension from 1765 to 2300. *Climatic Change (Special Issue)*, **109**, 213–241, doi:10.1007/s10584-011-0156-z.

Molteni, F., Stockdale, T., Balmaseda, M., Balsamo, G., Buizza, R., Ferranti, L., Magnusson, L., Mogensen, K., Palmer, T. and Vitart, F. (2011). The new ecmwf seasonal forecast system (system 4). *Ecmwf research department memorandum*, ECMWF, Shinfield Park, Reading, 656.

Morcrette, J.-J. (1991). Radiation and cloud radiative properties in the ecmwf operational weather forecast model. *J. Geophys. Res.*, **96D**, 9121–9132.

Morcrette, J.-J., Barker, H., Cole, J., Iacono, M. and Pincus, R. (2008). Impact of a new radiation package, mcrad, in the ecmwf integrated forecasting system. *Mon. Wea. Rev.*, **136**, 4773–4798.

Orr, A., Bechtold, P., Scinocca, J., Ern, M. and Janiskova, M. (2010). Improved middle atmosphere climate and forecasts in the ecmwf model through a nonorographic gravity wave drag parameterization. *J. Climate*, **23**, 5905–5926, doi:10.1175/2010JCLI3490.1.

Pachauri, R. K. and Reisinger, A. (2007). *Contribution of Working Groups I, II and III to the Fourth Assessment Report of the Intergovernmental Panel on Climate Change*. Cambridge University Press, United Kingdom and New York, NY, USA.

Poli, P., Hersbach, H., Tan, D., Dee, D., Thépaut, J.-N., Simmons, A., Peubey, C., Laloyaux, P., Komori, T., Berrisford, P., Dragani, R., Trémolet, Y., Holm, E., Bonavita, M., Isaksen, L. and Fisher, M. (2013). The data assimilation system and initial performance evaluation of the ecmwf pilot reanalysis of the 20th-century assimilating surface observations only (era-20c). *Ecmwf era report series*, ECMWF, Shinfield Park, Reading, 14.

Rayner, N. A., Kennedy, J., Smith, R. and Titchner, H. (2013). The met office hadley centre sea ice and sea-surface temperature data set, version 2, part 3: the combined analysis. **In preparation**.

Rayner, N. A., Parker, D. E., Horton, E. B., Folland, C. K., Alexander, L. V., Rowell, D. P., Kent, E. C. and Kaplan, A. (2003). analyses of sea surface temperature, sea ice, and night marine air temperature since the late nineteenth century. *J. Geophys. Res.*, **108 (D14)**, 4407, doi:10.1029/2002JD00267.

Rienecker, M. M., Suarez, M. J., Gelaro, R., Todling, R., Bacmeister, J., Liu, E., Bosilovich, M. G., Schubert, S. D., Takacs, L., Kim, G.-J., Bloom, S., Chen, J., Collins, D., Conaty, A., da Silva, A., Gu, W., Joiner, J., Koster, R., Lucchesi, R., Molod, A., Owens, T., Pawson, S., Pegion, P., Redder, C. R., Reichle, R., Robertson, F. R., Ruddick, A. G., Sienkiewicz, M. and Woollen, J. (2011). Merra: Nasas modern-era retrospective analysis for research and applications. *J. Climate*.

Sato, M., Hansen, J. E., McCormick, M. P. and Pollack, J. B. (1993). Stratospheric aerosol optical depth 1850-1990. *J. Geophys. Res.*, **98**, 22987–22994.

Schaaf, C., Gao, F., Strahler, A., Lucht, W., Li, X., Tsang, T., Strugnell, N., Zhang, X., Jin, Y., Muller, J.-P., Lewis, P., Barnsley, M., Hobson, P., Disney, M., Roberts, G., Dunderdale, M., Doll, C., d'Entremont, R., Hu, B., Liang, S., Privette, J. and Roy, D. (2002). First operational brdf, albedo nadir reflectance products from modis. *Remote Sensing Environm.*, **83**, 135–148.

Simmons, A. J., Jones, P. D., da Costa Bechtold, V., Beljaars, A. C. M., Kållberg, P. W., Saarinen, S., Uppala, S. M., Viterbo, P. and Wedi, N. (2004). Comparison of trends and low-frequency variability in cru, era-40 and ncep/ncar analyses of surface air temperature. *J. Geophys. Res.*, **109**, D24115, doi:10.1029/2004JD005306.

Simmons, A. J., Poli, P., Dee, D. P., Berrisford, P., Hersbach, H. and Peubey, C. (2013). Estimating lowfrequency variability and trends in atmospheric temperature from the erainterim reanalysis. *Draft paper available from ftp.ecmwf.int/pub/Simmons/ERA-Interim_temperature_7912.pdf.*

Simmons, A. J., Willett, K. M., Jones, P. D., Thorne, P. W. and Dee, D. P. (2010). Low-frequency variations in surface atmospheric humidity, temperature and precipitation: Inferences from reanalyses and monthly gridded observational datasets. *J. Geophys. Res.*, **115**, 22987–22994, doi:10.1029/2009JD012442.

Stickler, A., Grant, A. N., Ewen, T., Ross, T. F., Vose, R., Comeaux, J., Bessemoulin, P., Jylhä, K., Adam, W., Jeannet, P., Nagurny, A., Sterin, A., Allan, R., Compo, G., Griesser, T. and Brönnimann, S. (2010). The comprehensive historical upper air network (chuan). *Bull. Amer. Meteor. Soc.*, **91**, 741–751, doi:10.1175/2009BAMS2852.1.

Tanre, D., Geleyn, J.-F. and Slingo, J. M. (1984). First results of the introduction of an advanced aerosol-radiation interaction in the ECMWF low resolution global model. In H. E. Gerber and A. Deepak (Eds), *Aerosols and Their Climatic Effects*, pp. 133–177, A. Deepak Publ., Hampton, Va.

Taylor, K., Stouffer, R. and Meehl, G. (2012). An overview of cmip5 and the experiment design. *Bull. Amer. Meteor. Soc.*, **93**, 485–498, doi:10.1175/BAMS-D-11-00094.1.

Tegen, I., Hoorig, P., Chin, M., Fung, I., Jacob, D. and Penner, J. (1997). Contribution of different aerosol species to the global aerosol extinction optical thickness: Estimates from model results. *J. Geophys. Res.*, **102**, 23,895–23,915.

Titchner, H. A. and Rayner, N. (2013). The met office hadley centre sea ice and sea-surface temperature data set, version 2, part 2: sea-ice. **In preparation**.

Trenberth, K. E., Fasullo, J. T. and Kiehl, J. (2009). Earth's global energy budget. *Bull. Amer. Meteor. Soc.*, **90**, 311–323.

Trenberth, K. E., Fasullo, J. T. and Smith, L. (2005). Trends and variability in column integrated atmospheric water vapor. *Clim. Dynam.*, **24**, 741–758, doi:10.1007/s00382-005-0017-4.

Uppala, S. M., Kållberg, P. W., Simmons, A. J., Andrae, U., da Costa Bechtold, V., Fiorino, M., Gibson, J. K., Haseler, J., Hernandez, A., Kelly, G. A., Li, X., Onogi, K., Saarinen, S., Sokka, N., Allan, R. P., Andersson, E., Arpe, K., Balmaseda, A. M., Beljaars, A. C. M., van de Berg, L., Bidlot, J., Bormann, N., Caires, S., Chevallier, F., Dethof, A., Dragosavac, M., Fisher, M., Fuentes, M., Hagemann, S., Hólm, E., Hoskins, B. J., Isaksen, L., Janssen, P. A. E. M., Jenne, R., McNally, A. P., Mahfouf, J.-F., Morcrette, J.-J., Rayner, N. A., Saunders, R. W., Simon, P., Sterl, A., Trenberth, K. E., Untch, A., Vasiljevic, D., Viterbo, P. and Woollen, J. (2005). The era-40 re-analysis. *Quart. J. Roy. Meteor. Soc.*, **131**, 2961–3012, doi:10.1256/qj.04.176.

van Vuuren, D. P., Edmonds, J., Kainuma, M., Riahi, K., Thomson, A., Hibbard, K., Hurtt, G. C., Kram, T., Krey, V., Lamarque, J. F., Masui, T., Meinshausen, M., Nakicenovic, N., Smith, S. J. and Rose, S. K. (2011). The representative concentration pathways: an overview. *Climatic Change*, **109**, 5–31.

Wentz, F. J. (1997). A well-calibrated ocean algorithm for ssm/i. *J. Geophys. Res.*, **102**, 8703–8718, doi:10.1029/96JC01751.

Wentz, F. J. and Francis, E. A. (1992). Nimbus-7 smmr ocean products, 1979-1984. *Remote sensing systems technical report 033192*, Remote Sensing Systems, 1101 College Avenue, Suite 220, Santa Rosa, CA 95404, 033192.

Willett, K. M., Berry, D. and Simmons, A. J. (2013). Global climate. hydrological cycle] surface humidity [in state of the climate in 2012]. *Bull. Amer. Meteor. Soc.*, **94**, S18–S19.

Willett, K. M., Jones, P. D., Gillett, N. P. and Thorne, P. W. (2008). Recent changes in surface humidity: Development of the hadcruh dataset. *J. Climate*, **21**, 5364–5383, doi:10.1175/2008JCLI2274.1.

Woodruff, S. D., Worley, S. J., Lubker, S., Ji, Z., Freeman, J. E., Berry, D., P. Brohan, E. K., Reynolds, R., Smith, S. and Wilkinson, C. (2011). Icoads release 2.5: Extensions and enhancements to the surface marine meteorological archive. *Int. J. Climatol.*, **31**, 951–967, doi:10.1002/joc.2103.